Computing Interface Motion in Compressible Gas Dynamics

W. MULDER* AND S. OSHER[†]

Department of Mathematics, University of California, Los Angeles, California 90024

AND

JAMES A. SETHIAN[‡]

Department of Mathematics, University of California, Berkeley, California 94720

A "Hamilton–Jacobi" level set formulation of the equations of motion for propagating interfaces has been introduced recently by Osher and Sethian. This formulation allows fronts to self-intersect, develop singularities, and change topology. The numerical algorithms based on this approach handle topological merging and breaking naturally, work in any number of space dimensions, and do not require that the moving front be written as a function. Instead, the moving front is embedded as a particular level set in a fixed domain partial differential equation. Numerical techniques borrowed from hyperbolic conservation laws are then used to accurately capture the complicated surface motion that satisfies the global entropy condition for propagating fronts given by Sethian. In this paper, we analyze the coupling of this level set formulation to a system of conservation laws for compressible gas dynamics. We study both conservative and non-conservative differencing of the level set function and compare the two approaches. To illustrate the capability of the method, we study the compressible Rayleigh–Taylor and Kelvin–Helmholtz instabilities for air–air and air–helium boundaries. We perform numerical convergence studies of the method over a range of parameters and analyze the accuracy of this approach applied to these problems. © 1992 Academic Press, Inc.

A variety of physical phenomena involve propagating interfaces. The interface (or interfaces) separate regions which may differ according to their density, viscosity, or chemical type. The complexity of the motion of the interface can range from the particularly simple case of passive advection of two different colors, to problems in flame propagation and dendrite solidification, in which there is an intricate feedback mechanism between the local properties of the front and the physics on either side of it.

Recently, a new set of algorithms for following propagating interfaces has been developed. In [47], a Hamilton–Jacobi level set formulation for moving interfaces was introduced. These algorithms handle topological merging and breaking naturally, work in any number of space dimensions, and do not require that the moving front be written as a function. Instead, the moving front is embedded as a particular level set in a fixed domain partial differential equation. Numerical techniques borrowed from hyperbolic conservation laws are then used to accurately calculate the correct solution which satisfies the global entropy condition for propagating fronts given in [60].

These schemes have been used to model a variety of problems in front motion, flame propagation, and the geometry of moving surfaces, see [47, 60, 61]. Following the introduction of this level set formulation for moving fronts, it has also been used for theoretical analysis of motion by mean curvature in [9, 18] and for constructing minimal surfaces [59].

In this paper, we analyze the coupling of this level set formulation to a system of conservation laws for compressible gas dynamics. We consider two different approaches. In one approach, the level set function is solved in non-conservative form, using the velocity obtained from conservative differencing of the standard hyperbolic system. In another approach, we directly incorporate the level set formulation into a system of five conservation laws, in which the moving front becomes one extra variable in the flow solver. In both the conservative and non-conservative settings, we also analyze a degenerate initialization of our level set approach, known as the color function. We then compare the various approaches and discuss how the physics of the problem suggest the appropriate approach.

As application, we study the compressible Rayleigh–Taylor and Kelvin–Helmholtz instabilities for air–air and air–helium boundaries. We compute the position of the moving interface, showing the development of plumes and rolls in the Rayleigh–Taylor instability and the rolling up of vortex structures in the Kelvin–Helmholtz instability. We perform numerical convergence studies of the method over a range of parameters and analyze the accuracy of this approach applied to these problems.

I. PHYSICAL PROBLEMS

In this section, we discuss the two physical problems under investigation.

A. *Physical Problems*

The Rayleigh–Taylor instability occurs when a light fluid pushes a heavier one. Imagine a horizontal interface, in which a fluid with density ρ_1 lies above a fluid with density ρ_2. Here we assume that gravity is pointing downwards. If $\rho_1 < \rho_2$, the interface is stable and the two fluids remain motionless. Small perturbations in the initial shape of the interface remain bounded. On the other hand, if $\rho_1 > \rho_2$, the interface is unstable. Small perturbations in the initial shape grow as the heavier fluid on the top pushes through these perturbations and long fingers of the heavier fluid reach down into the lighter fluid. At the same time, plumes of the lighter fluid grow upward. The initial growth rate of the perturbations is exponential. Experimental observations indicate that the heavier fluid forms long "spikes" as it reaches into the lighter fluid, while the rising light fluid forms rounded tops, or "bubbles." The length of the interface increases dramatically and can break into several parts, developing bubbles. Some examples where this instability can occur are in the collapse of a massive star, the laser implosion of deuterium–tritium fusion targets, and the electromagnetic implosion of a metal liner. One of the most straightforward examples is the novelty-store toy in which fluids of differing densities are trapped between two glass plates. By upending the apparatus, the lighter fluid rises to the top by forming long spikes in the interface. Bubbles can break off from the interface and later merge with other bubbles. The interface between the two fluids becomes highly complex, breaking into numerous different parts with wildly varying shapes.

In their most complicated form, the equations of motion are the equations of full viscous, compressible flow plus interface effects. Some important factors controlling the growth of instability are: (1) the density ratio, which governs the growth of small amplitude perturbation; (2) surface tension, which stablizes wavelengths shorter than a critical wavelength; (3) the viscosity, which reduces growth rate and regularizes the flow; (4) compressibility, which reduces growth rate; and (5) heterogeneity, which can excite instabilities of various wavelengths.

The Kelvin–Helmholtz instability occurs when one fluid is moving at a different rate relative to another. Imagine one fluid atop another, moving at different speeds initially parallel to the interface. The initial horizontal interface rolls up into large vortical structures, which serve to entrap the fluid. In compressible gas flow, the Kelvin–Helmholtz instability can be seen when a jet of fluid is injected into another, producing large vortical structures which roll up the interface between the two fluids. Another example is provided by parallel shear flow for incompressible fluids, which can be modeled through the study of vortex sheets. Here, the vorticity is zero everywhere except along an infinitely thin line or curve. A good example is flow around the trailing edge of a wing, which forms a vortex sheet whose strength depends on the given wing design. The ensuing motion and rollup of the vortex sheet affects both the drag on the wing and the flight of following aircraft.

For some experimental studies of these phenomena, we refer the interested reader to [12, 16, 28, 29, 37, 38, 51, 53, 55]. In addition, we draw the reader's attention to the recent experiment on the three-dimensional Rayleigh–Taylor instabilities described in [29]. This paper contains some fascinating photographs of three-dimensional instabilities in circular tubes and direct comparison with solutions from linear and non-linear theory developed in [28]. For studies of the theoretical aspects of Rayleigh–Taylor and Kelvin–Helmholtz instabilities, a possible starting point may be found in [4, 5, 6, 8, 20, 27, 34, 40, 41, 44, 45, 50, 54, 56, 58, 65].

B. *Numerical Studies*

Two different types of numerical methods are often employed for computing interface problems in fluid mechanics. The first, or "Eulerian" type, compute the full Navier–Stokes equations in both fluids. In these techniques, the finite difference approximations are typically employed across the entire domain. The second, or "Lagrangian" type, reduce the equations of motion to equations for the interface itself. Here, one ofter uses markers to track the interface. One example in this category are vortex methods, which rely on a discrete approximation to a boundary integral along the interface, see [3, 11, 18, 30–33, 40, 52, 65]. An excellent overview of some work on the Rayleigh–Taylor instability is due to Sharp [62]. Other calculations include [1, 2, 15, 19, 26, 42, 43, 46, 69]. Some particularly beautiful calculations of compressible jets may be found in [7, 68].

Hybrid "Eulerian–Lagrange" methods have also been employed. These methods are used in some of the earliest numerical calculations of the Rayleigh–Taylor instability, which were performed by Harlow and Welch [23]. In these

calculations, the marker-and-cell method was introduced, in which a finite difference scheme is used to solve the full Navier–Stokes equations. One of the two fluids, say Type 1, is tracked by placing marker points at the centers of cells initially containing the chosen fluid. These markers are then advected with the computed fluid velocity. At subsequent times, cells are divided into three types: (a) those containing marker particles and whose neighboring cells contain marker particles (Type 1 fluid); (b) those not containing marker particles and whose neighboring cells also do not contain marker particles (Type 2 fluid); and (c) surface cells which must contain the boundary. Using this technique, a moving fluid interface was tracked. An extension of this technique was used in [14] to track the growth of a single mode of the Rayleigh–Taylor instability, showing the development of a large bubble and accompanying spike.

The most involved calculations using a combination Eulerian–Lagrangian scheme which couples the Navier–Stokes equations to a method for tracking fronts is the front tracking technology due to Glimm *et al.* [21, 22]. In this work, the compressible Navier–Stokes equations are solved in the whole domain, and the interface is tracked through a set of marker particles on the moving interface. A variety of calculations of bubble and spike development for the Rayleigh–Taylor problem may be found in [21, 22, 63]. Another method for following moving interfaces is given in [36].

II. EQUATIONS OF MOTION FOR PROPAGATING INTERFACES

A. *Statement of Problem*

In the most general form, consider a propagating hyper-surface $S(t)$ (that is, a curve in two space dimensions or a surface in three space dimensions) separating two regions in the domain. Here, t is time, and $S(t)$: $[0, \infty) \rightarrow R^N$, $N = 2, 3$. Suppose that $S(t)$ propagates normal to itself with speed F. F may vary along the interface $S(t)$ and depend on such factors as the position of the front $S(t)$, the direction of the normal $\mathbf{n}(t)$, the local curvature $K(t)$, as well as the time t. Note that the dependence of F on the position $S(t)$ can generate tremendous complexity, since the physics on both sides of the interface may enter into the determination of F. Our goal is a numerical algorithm that follows the motion of $S(t)$.

It might seem most natural to formulate equations of motion by parameterizing the hypersurface and describing the evolution of the interface in terms of coordinate-free "Lagrangian" front properties, such as the local normal $\mathbf{n}$ and curvature K. Indeed, a standard numerical method for tracking moving fronts relys on discretizing such a parameterization with marker particles whose motion is determined by a discrete approximation to the appropriate

equations of motion, see [70]. As shown in [60, 61], such techniques can encounter considerable difficulties when sharp corners develop in the propagating interfaces or when the interface changes topology. A rigorous explanation of the inherent instability of this approach is given in the appendix of [47]. Instead, we consider an "Eulerian" formulation of the equations of motion which is more amenable to numerical approximation. The details of this formulation were first presented in [47].

B. *Eulerian Formulation*

Given a closed hypersurface $\Gamma(t)$, we wish to produce an Eulerian formulation for the motion of the hypersurface propagating along its normal direction with speed F. We motivate the Eulerian formulation by a simple example, taken from [61].

Let $\Gamma(t)$ be a unit circle in R^2 propagating outward with constant speed $F \equiv 1$. Obviously, the solution at any time t is just a circle with radius $(t + 1)$. Rather than describe the motion of this circle, we consider the motion of a surface $z = \psi(x, y, t)$ in R^3. The level set $\psi = 0$ of this surface is just the set of points in the x–y plane corresponding to the propagating curve $\Gamma(t)$. That is,

$$\Gamma(t) = ((x, y) \,|\, \psi(x, y, t) = 0). \tag{2.1}$$

Thus, we have matched the motion of the front $\Gamma(t)$ in R^2 with the evolution of a function $z = \psi(x, y, t)$ in R^3. At this point, we must describe how to

(1) Construct the initial value $\psi(x, y, 0)$

(2) Derive the equations of motion for the evolving surface.

We shall do this in some generality, referring to an $(N - 1)$-dimensional hypersurface with arbitrary speed function F.

C. *Construction of the Initial Value for ψ*

Suppose we are given a closed, propagating $(N - 1)$-dimensional hypersurface $\Gamma(t)$, where $\Gamma(t)$: $[0, \infty) \rightarrow R^N$. A straightforward technique for constructing the initial front $\psi(\bar{x}, t = 0)$, where $\bar{x} \in R^N$, is to let

$$\psi(\bar{x}, t = 0) = \pm d, \tag{2.2}$$

where d is the distance from $\bar{x}$ to $\Gamma(t = 0)$, and the plus (minus) sign is chosen if the point $\bar{x}$ is outside (inside) the initial hypersurface $\Gamma(t = 0)$. Thus, we have an initial function $\psi(x, t = 0)$: $R^N \rightarrow R$ with the property that

$$\Gamma(t = 0) = (\bar{x} \,|\, \psi(\bar{x}, t = 0) = 0).$$

Our goal is to now produce an equation for the evolving function $\psi(\bar{x}, t)$ which contains the embedded motion of $\Gamma(t)$ as the level set $\psi = 0$.

D. Derivation of the Evolution Equation for ψ

We are given a propagating hypersurface $\Gamma(t)$ and a speed function F at each point of the propagating hypersurface. Let $\bar{x}(t)$, $t \in [0, \infty)$, be the path of a point on the propagating front. That is, $\bar{x}(t = 0)$ is a point on the initial front $\Gamma(t = 0)$, and $|\bar{x}_t| = F(\bar{x}(t))$ and the vector $\bar{x}_t$ is in the direction normal to the front at $\bar{x}(t)$. Since the evolving function ψ is always zero on the propagating hypersurface, we must have

$$\psi(\bar{x}(t), t) = 0. \tag{2.3}$$

By the chain rule,

$$\psi_t + \sum_{i=1}^{N} \psi_{x_i} x_{i_t} = 0, \tag{2.4}$$

where x_i is the ith component of $\bar{x}$. Let $(u_1, u_2, ..., u_N) = (x_{1_t}, x_{2_t}, ..., x_{N_t})$. Since

$$\sum_{i=1}^{N} \psi_{x_i} x_{i_t} = (\psi_{x_1}, \psi_{x_2}, ..., \psi_{x_N})$$
$$\cdot (u_1, u_2, ..., u_N) = F(\bar{x}(t)) |\nabla\psi|, \tag{2.5}$$

we then have the evolution equation for ψ, namely,

$$\psi_t + F |\nabla\psi| = 0. \tag{2.6}$$

We refer to this as a Hamilton–Jacobi "type" equation because, for speed function F identically constant, we obtain a standard Hamilton–Jacobi equation.

To repeat, the position of the propagating hypersurface $\Gamma(t)$ is given as the level set

$$\Gamma(t) = \{\bar{x} \mid \psi(\bar{x}, t) = 0\}, \tag{2.7}$$

where $\psi(\bar{x}, t)$ is the solution to the Hamilton–Jacobi-type equation

$$\begin{aligned} \psi_t + F |\nabla\psi| &= 0 \\ \psi(\bar{x}, t = 0) &= \pm \text{distance } \Gamma(t = 0). \end{aligned} \tag{2.8}$$

E. Advantages to the Eulerian Formulation

There are three major advantages to this Eulerian Hamilton–Jacobi formulation. First, the evolving function $\psi(\bar{x}, t)$ always remains a function for reasonable F. However, the level surface $\psi = 0$, and hence the propagating

hypersurface $\Gamma(t)$ may change topology, break, merge, and form sharp corners as the function ψ evolves. As an example, consider two circles in R^2 expanding outward. The initial function $\psi(\bar{x}, t = 0)$ is a double-humped function which is Lipshitz continuous, but not everywhere differentiable. As this function evolves according to Eqs. (2.7)–(2.8) the topology of the level set $\psi = 0$, corresponding to the propagating hypersurface $\Gamma(t)$, can change. For example, as the two circles expand, they meet and merge into a single closed curve with two corners. This is reflected in the change of topology of the level set $\psi = 0$ in the propagating function.

The second major advantage of this Eulerian formulation concerns numerical approximation. Because $\psi(\bar{x}, t)$ remains a function as it evolves, we may use a discrete grid in the domain of $\bar{x}$ and substitute finite difference approximations for the spatial and temporal derivatives.

Finally, the Eulerian Hamilton–Jacobi formulation extends in an obvious way to moving surfaces in three space dimensions. All of the numerical methodology described below is easily generalized, with none of the complicated bookkeeping that plagues marker particle technology and volume of fluid methods.

F. Extension of F Off te Level Surface $\psi = 0$

As mentioned earlier, F may depend on such factors as the position of the front and the local curvature. We point out a somewhat subtle issue that results from our Eulerian formulation. We have formed an extension of F off the propagating hypersurface to all of space. That is, the equation

$$\psi_t + F |\nabla\psi| = 0$$

applies to each level set $\psi = C$, and thus we have implicitly assumed that is a function in $R^N \times [0, \infty) : F(\bar{x}, t)$ such that

$$F(\bar{x}, t) = F(\Gamma(t)) \qquad \text{for} \quad (\bar{x}, t) \in \Gamma(t).$$

How does one extend F off the propagating hypersurface $\Gamma(t)$ to the entire domain? In previous work (see [47, 61]), the function F depended on the local curvature of the propagating level set $\psi = 0$. In this case, since the local curvature could be calculated for the entire family of level sets covering the domain, it is straightforward to extend F by using the value of the curvature at a point $\bar{x}$ in the domain determined by the particular level set passing through that point.

In the Rayleigh–Taylor and Kelvin–Helmholtz problems considered here, the level set $\psi = 0$ is carried by the underlying fluid advection, and thus the speed function F depends only on the position of the level set $\psi = 0$. Thus, we

may quite naturally extend the speed F to the entire domain by moving each level set by the underlying fluid.

In more complicated cases, the speed function can depend on such factors as the local normal, boundary integrals along the level set $\psi = 0$ and other factors. In such cases, the extension of F off the propagating hypersurface to the entire domain is not straightforward. The most complicated interface motion studied to date using this Hamilton–Jacobi approach is dendritic solidification, see [62]. In that work, the motion of the front and extension of F requires the global evaluation of a time history-dependent boundary integral along the boundary. For details, see [62].

III. COMPRESSIBLE FLOW AND PROPAGATING INTERFACES

In this section, we discuss how to couple the level set formulation for a propagating interface to a system of conservation laws. To begin, consider the system of equations which describe compressible flow, namely,

$$\tilde{\mathbf{q}}_t + [\tilde{\mathbf{F}}(\tilde{\mathbf{q}})]_x + [\tilde{\mathbf{G}}(\tilde{\mathbf{q}})]_y = \tilde{\mathbf{H}}(\tilde{\mathbf{q}}), \qquad (3.1)$$

where the vector $\tilde{\mathbf{q}}$ is defined by

$$\tilde{\mathbf{q}} = \begin{pmatrix} \rho \\ \rho u \\ \rho v \\ \rho \varepsilon \end{pmatrix} \qquad (3.2)$$

Here, $\rho = \rho(x, y, t)$ is the density, $u = u(x, y, t)$ is the velocity in the x direction, $v = v(x, y, t)$ is the velocity in the y direction, and $\varepsilon = \varepsilon(x, y, t)$ is the specific energy of the system. The flux functions $\tilde{\mathbf{F}}(\tilde{\mathbf{q}})$ and $\tilde{\mathbf{G}}(\tilde{\mathbf{q}})$ are given by

$$\tilde{\mathbf{F}}(\tilde{\mathbf{q}}) = \begin{pmatrix} \rho u \\ \rho u^2 + P \\ \rho uv \\ \rho u\varepsilon + uP \end{pmatrix}, \qquad \tilde{\mathbf{G}}(\tilde{\mathbf{q}}) = \begin{pmatrix} \rho v \\ \rho uv \\ \rho v^2 + P \\ \rho v\varepsilon + vP \end{pmatrix}. \qquad (3.3)$$

The forcing function $\tilde{\mathbf{H}}(\tilde{\mathbf{q}})$ depends on the particular problem under study. For the Rayleigh–Taylor problem, we assume that gravity g is pointing up (the positive y direction), and thus we have

$$\tilde{\mathbf{H}}(\tilde{\mathbf{q}}) = \begin{pmatrix} 0 \\ 0 \\ \rho g \\ \rho vg \end{pmatrix}. \qquad (3.4)$$

For the Kelvin–Helmholtz problem, we assume that

$$\tilde{\mathbf{H}}(\tilde{\mathbf{q}}) = \begin{pmatrix} 0 \\ 0 \\ 0 \\ 0 \end{pmatrix}. \qquad (3.5)$$

Finally, we use the equation of state to link the pressure P and the density, namely,

$$P = (\gamma - 1)\,\rho(\varepsilon - 1/2(u^2 + v^2)), \qquad (3.6)$$

where here we have used the typical γ-gas law. A more complete gas law would add only technical and not conceptual difficulties to the numerical method described below.

Our goal now is to incorporate interface motion in this setting. Let Ω_1 and Ω_2 be two regions in R^2 separated by a curve $\Gamma(t = 0)$ which is a small perturbation of a horizontally straight line. Suppose Ω_1 is above Ω_2, and that the density in Ω_1 is less than that in Ω_2. The system of conservation laws described above apply in both Ω_1 and Ω_2, with possibly different γ-law equations of state. Suppose the location of the propagating interface $\Gamma(t)$ is given by the level set $\psi(x, y, t) = 0$. Then the full motion of the two regions can be viewed as a single system of conservation laws, which may be solved by appropriate finite difference approximations. What remains is to couple the equations of motion for ψ to the system given in Eq. (3.1).

A. Non-conservative Differencing for ψ

For Eq. (2.4), we have

$$\psi_t + u\psi_x + v\psi_y = 0, \qquad (3.7)$$

where $u = u_1$, $v = u_2$, and ψ is the evolving function $\psi(x, y, t)$ such that

$$\Gamma(t) = ((x, y) \mid \psi(x, y, t) = 0). \qquad (3.8)$$

Then one approach is to solve Eq. (3.7), which is in non-conservative form, using the velocities (u, v) obtained from the hyperbolic system given in Eq. (3.1).

B. Conservative Differencing for ψ

Alternatively, we may put the equation of motion for the evolving function ψ in conservation form. We have

$$(\rho\psi)_t + (\rho u\psi)_x + (\rho v\psi)_y$$
$$= [\rho_t + (\rho u)_x + (\rho v)_y]\psi + \rho[\psi_t + u\psi_x + v\psi_y]$$
$$= 0 + 0 = 0. \qquad (3.9)$$

For piecewise continuous ψ, the Rankine–Hugoniot jump conditions for this equation are the same as for the conservation of mass equation (Eq. (3.1)). Thus, we may write a single system of conservation laws for the motion of the fluid in each region and the level set function ψ, namely,

$$\mathbf{q}_t + [\mathbf{F}(\mathbf{q})]_x + [\mathbf{G}(\mathbf{q})]_y = \mathbf{H}(\mathbf{q}), \qquad (3.10)$$

where

$$\mathbf{q} = \begin{pmatrix} \rho \\ \rho u \\ \rho v \\ \rho \varepsilon \\ \rho \psi \end{pmatrix} \qquad (3.11)$$

$$\mathbf{F}(\mathbf{q}) = \begin{pmatrix} \rho u \\ \rho u^2 + P \\ \rho u v \\ \rho u \varepsilon + u P \\ \rho u \psi \end{pmatrix}, \qquad \mathbf{G}(\mathbf{q}) = \begin{pmatrix} \rho v \\ \rho u v \\ \rho v^2 + P \\ \rho v \varepsilon + v P \\ \rho v \psi \end{pmatrix} \qquad (3.12)$$

$$\mathbf{H}(\mathbf{q}) = \begin{pmatrix} 0 \\ 0 \\ \rho g \\ \rho v g \\ 0 \end{pmatrix} \text{Rayleigh–Taylor}$$

$$(3.13)$$

$$\mathbf{H}(\mathbf{q}) = \begin{pmatrix} 0 \\ 0 \\ 0 \\ 0 \\ 0 \end{pmatrix} \text{Kelvin–Helmholtz.}$$

All that remains is to formulate the equation of state. We define the pressure P by

$$P = (\gamma(\psi) - 1)\, \rho(\varepsilon - 1/2(u^2 + v^2)), \qquad (3.14)$$

where

$$\gamma(\psi) = \begin{pmatrix} \gamma_1 & \psi > 0 \\ \gamma_2 & \psi < 0 \\ ? & \psi = 0 \end{pmatrix}. \qquad (3.15)$$

Away from $\psi = 0$, this is a conventional hyperbolic system of conservation laws with the standard propagation velocities of gas dynamics, and a triple linear degeneracy corresponding to the particle velocity. At $\psi = 0$, the fluxes are discontinuous, and it is not obvious what the correct conditions should be: this is reflected in the question mark

"?" in Eq. (3.15). In Section 5 we derive the appropriate condition at $\psi = 0$ and its numerical implementation.

We point out here that the extra work in computing the front is rather small. To solve the fundamental system of equations involves the use of a good numerical approximation to the system of conservation laws in two space dimensions. Computing the interface motion via the level set function requires either adding one more unknown to the system, namely $(\rho \psi)$, in a way that preserves the hyperbolic conservation law structure, or solving a coupled equation in non-conservative form. In either case, the same finite difference grid lattice is used and requires only one more array in the above data structures.

IV. SOLVING HYPERBOLIC SYSTEMS

A. General Outline

In this section, we lay the groundwork for our numerical methods. The field of hyperbolic solvers has grown rapidly in the past ten years, and good overviews of the material may be found in the review articles [49, 57] and the references therein. Here, we give a brief flavor of the basic idea for those unfamiliar with the field.

The basic idea behind these methods is as follows. Consider, as a simple example, the n component linear hyperbolic system in one space variable, namely

$$\mathbf{u}_t + [\mathbf{a}(\mathbf{u})]_x = 0. \qquad (4.1)$$

Performing the differentiation, we then have

$$\mathbf{u}_t + \left[\frac{\partial \mathbf{a}(\mathbf{u})}{\partial \mathbf{u}} \right] \bar{u}_x = \mathbf{u}_t + A \bar{u}_x = 0, \qquad (4.2)$$

where $A = [\partial \mathbf{a}/\partial \mathbf{u}]$ is the (constant) $m \times m$ Jacobian matrix. Suppose T diagonalizes A. Then

$$TAT^{-1} = \Lambda, \qquad (4.3)$$

where Λ is diagonal. Then if we define the vector

$$\tilde{\mathbf{u}} = T\mathbf{u}, \qquad (4.4)$$

we can premultiply Eq. (4.2) by T and postmultiply by T^{-1} to obtain the decoupled diagonal system

$$\tilde{\mathbf{u}}_t + \Lambda \tilde{\mathbf{u}}_x = 0. \qquad (4.5)$$

Consider now the ith component of the above diagonal system, namely

$$(\tilde{u}_k)_t + \Lambda_k (\tilde{u}_k)_x = 0. \qquad (4.6)$$

We may solve this equation exactly, since Λ_k is a constant, and retrieve the solution $\mathbf{u}$ by letting

$$\mathbf{u} = \mathbf{T}^{-1}\tilde{\mathbf{u}}. \tag{4.6}$$

The strategy behind numerical algorithms for more general non-linear hyperbolic conservation laws is a time and space discretization of a non-linear version of the above process. Consider a lattice of points $x_i = ih$, $i = \cdots -3, -2, -1, 0, 1, 2, 3, \ldots$ and the general system of the form

$$\mathbf{u}_t + \left[\frac{\partial \mathbf{a}(\mathbf{u})}{\partial \mathbf{u}}\right]\bar{u}_x = \mathbf{u}_t + \mathbf{A}\bar{u}_x = 0, \tag{4.7}$$

where now $\mathbf{A}(\bar{u})$ is nonlinear. Let $\mathbf{u}_j^n$ denote the approximate solution at time $n\,\Delta t$ at point x_j. In order to go from the solution at time $n\,\Delta t$ to the solution at time $(n+1)\,\Delta t$, at each point x_i we compute the eigenvectors of the Jacobian matrix $\mathbf{A}(\mathbf{u})$ to construct the diagonalizing matrices $\mathbf{T}$ and $\mathbf{T}^{-1}$. The matrices $\mathbf{A}$ and $\mathbf{T}$, $\mathbf{T}^{-1}$ are functions of $\mathbf{u}$. Their values at an intermediate state between $\mathbf{u}_i$ and $\mathbf{u}_{i+1}$, denoted as $\mathbf{u}_{i+1/2}$ at $x_{i+1/2}$, are approximated in Section 5 and used in the numerical procedure to update $\mathbf{u}$ as follows: At each point $x_{i+1/2}$, we have a local Riemann problem, which assumes a constant left initial state and a constant right initial state. Imagine then, that at each point $x_{i+1/2}$ at time $n\,\Delta t$, we consider the local Riemann problem which has initial state $\mathbf{u}_{i+1/2}^{+(n)}$ on the right and $\mathbf{u}_{i+1/2}^{-(n)}$ on the left (we postpone until later the calculation of these intermediate mesh values). Using approximate Riemann solvers, we solve this initial value problem for time step Δt, where Δt is chosen small enough that waves traveling from neighboring Riemann problems do not interact. The matrices $\mathbf{A}(\mathbf{u})$ and $\mathbf{T}(\mathbf{u})$ play a key role in the approximate solutions to the Riemann problem. Details of these ideas may be found in [49, 57].

B. The Equations of Motion for Gas Flow and Interface Motion

Following the above outline, the first task is to compute the eigenvalues and eigenvectors of $\mathbf{A}$, which is the Jacobian matrix of $\mathbf{F}(\mathbf{q})$. There is a similarity between our set of five conservation laws (Eqs. (3.10)–(3.11)) and the equations of two-component inviscid gas flow studied by [35]. In those equations, the level set function ψ is replaced by the mass fraction Y of species one. In addition, the quantity γ defined in Eq. (3.15) is no longer a piecewise constant function of ψ, but instead, for the two-component mixture case, is given by (see [35])

$$\gamma = \frac{Yc_{v_1}\gamma_1 + (1-Y)c_{v_2}\gamma_2}{Yc_{v_1} + (1-Y)c_{v_2}}, \tag{4.8}$$

where c_{v_i} is the specific heat at constant volume of species i.

For simplicity of exposition we compute the one-space-dimensional Jacobian, where we set $v \equiv 0$ and neglect the ρv equation in (Eqs. (3.10)–(3.11)). We note that γ is a function of Y for our problem and a function of ψ for the two-component problem. Using conserved variables, we may view

$$\gamma = \gamma\left(\frac{\rho Y}{\rho}\right) \quad \text{(two component gases)} \tag{4.9}$$

or

$$\gamma = \gamma\left(\frac{\rho\psi}{\rho}\right) \quad \text{(level set, immiscible problem).} \tag{4.10}$$

We let ϕ denote either Y or ψ for the two problems and obtain the Jacobian as in [35]

$$\frac{\partial \mathbf{F}}{\partial \mathbf{q}} = \begin{cases} 0 & 1 & 0 & 0 \\ \left(\frac{\gamma-3}{2}\right)u^2 - \phi X & (3-\gamma)u & (\gamma-1) & X \\ \left(\frac{\gamma-1}{2}\right)u^3 - uH - u\phi X & H-(\gamma-1)u^2 & \gamma u & uX \\ -u\phi & \phi & 0 & u \end{cases}. \tag{4.11}$$

Here, the enthalpy H is defined by

$$H = \frac{\rho\varepsilon + p}{\rho} \tag{4.12}$$

and

$$X = \frac{p}{\gamma-1}\frac{\gamma}{\rho}. \tag{4.13}$$

The eigenvalues of A are

$$\lambda_1 = u - c, \quad \lambda_2 = u = \lambda_3, \quad \lambda_4 = u + c, \tag{4.14}$$

where

$$c = \sqrt{\gamma p/\rho}. \tag{4.15}$$

A set of right eigenvectors is

$$r_1 = \begin{cases} 1 \\ u-c \\ H-uc \\ \phi \end{cases}, \quad r_2 = \begin{cases} 1 \\ u \\ \frac{u^2}{2} \\ \phi \end{cases} \tag{4.16}$$

$$r_3 = \begin{cases} 0 \\ 0 \\ -\frac{X}{\gamma-1} \\ 1 \end{cases}, \quad r_4 = \begin{cases} 1 \\ u+c \\ H+uc \\ \phi \end{cases}. \tag{4.17}$$

For our definition of $\gamma(\psi)$, $\psi X = 0$, and

$$X = \frac{p}{(\gamma - 1)\rho} \delta(\psi - 0)[\gamma_2 - \gamma_1]. \qquad (4.18)$$

Obviously, $\delta(\psi - 0)$ must be approximated numerically. We shall describe this in the next section.

C. Approximate Riemann Solvers

We must now solve the Riemann problem that occurs in the decoupled diagonalized system. We use second-order TVD schemes, which can be based on either the true solution to the Riemann problem (Godunov's scheme), or, more likely, an approximate Riemann solver, e.g., Roe's [57], Osher's [49], or van Leer's [67].

For our problem, the simplest scheme is van Leer's, since it is based on a flux splitting

$$f_{VL}(\mathbf{q}_L, \mathbf{q}_R) = f^+(\mathbf{q}_L) + f^-(\mathbf{q}_R). \qquad (4.19)$$

The eigenvalues of $\partial f_+ / \partial \mathbf{q}$ ($\partial f_- / \partial \mathbf{q}$) are all nonnegative (nonpositive). Each typically has one zero and two nonzero eigenvalues. However, there is no "switching" across the point $u = 0$, thus the scheme is relatively viscous near stagnation points. This will be important in the solution of the Rayleigh–Taylor and Kelvin–Helmholtz problems.

For Osher's scheme

$$\hat{f}_O(\mathbf{q}_L, \mathbf{q}_R) = \frac{1}{2}[f(\mathbf{q}_L) + f(\mathbf{q}_R)]$$

$$- \frac{1}{2} \int_{\mathbf{q}_L}^{\mathbf{q}_R} \left| \frac{\partial f}{\partial \mathbf{q}}(\mathbf{q}) \right| d\mathbf{q}, \qquad (4.20)$$

where the integral is taken along successive paths parallel to the right eigenvectors of $\partial f / \partial \mathbf{q}$.

The construction here is simplified by requiring that the Riemann invariants be constant along each path. This leads to a single equation for a single unknown for an intersection point. It can be shown that Newton's method globally converges for this (details elsewhere).

Roe's scheme can be written as

$$\hat{f}_R(\mathbf{q}_L, \mathbf{q}_R) = \frac{1}{2}[f(\mathbf{q}_L) + f(\mathbf{q}_R)]$$

$$- \frac{1}{2}|\mathbf{A}_{LR}| (\mathbf{q}_R - \mathbf{q}_L), \qquad (4.21)$$

where $\mathbf{A}_{LR} = A(\mathbf{q}_L, \mathbf{q}_R)$ is a matrix satisfying

$$f(\mathbf{q}_L) - f(\mathbf{q}_R) = \mathbf{A}_{LR}(\mathbf{q}_L - \mathbf{q}_R). \qquad (4.22)$$

It turns out that for γ law gas dynamics, $\mathbf{A}_{LR}$ can be chosen to be the Jacobian matrix evaluated at some intermediate state $\mathbf{q}_{LR}$ known as the "Roe average of $\mathbf{q}_L$, $\mathbf{q}_R$." This cannot

be done for the system here. However, in [35] a Roe matrix for two-component flow was constructed which is very close to the Jacobian at the Roe average. The expression is

$$\frac{\partial \mathbf{F}}{\partial \mathbf{q}} = \begin{pmatrix} 0 & 1 & 0 & 0 \\ \dfrac{(\hat{\gamma} - 3)}{2} \hat{u}^2 - \hat{Y}\hat{X} & (3 - \hat{\gamma})\hat{u} & \hat{\gamma} - 1 & \hat{X} \\ -\hat{u}\hat{H} + \dfrac{(\hat{\gamma} - 1)}{2} \hat{u}^3 \hat{u}\hat{Y}\hat{X} & \hat{H} - (\hat{\gamma} - 1)\hat{u}^2 & \hat{\gamma}\hat{u} & \hat{u}\hat{X} \\ -\hat{u}\hat{Y} & \hat{Y} & 0 & \hat{u} \end{pmatrix}, \qquad (4.23)$$

where the averaged state $\hat{\mathbf{q}} = (\hat{\rho}, \hat{\rho}\hat{u}, \hat{E}, \hat{\rho}\hat{Y})^{\mathrm{T}}$ is defined by

$$\hat{\rho} = \frac{\rho_L \sqrt{\rho_L} + \rho_R \sqrt{\rho_R}}{\sqrt{\rho_L} + \sqrt{\rho_R}} = \sqrt{\rho_L \rho_R} \qquad (4.24)$$

$$\hat{u} = \frac{u_L \sqrt{\rho_L} + u_R \sqrt{\rho_R}}{\sqrt{\rho_L} + \sqrt{\rho_R}} \qquad (4.25)$$

$$\hat{H} = \frac{H_L \sqrt{\rho_L} + H_R \sqrt{\rho_R}}{\sqrt{\rho_L} + \sqrt{\rho_R}} \qquad (4.26)$$

$$\hat{Y} = \frac{Y_L \sqrt{\rho_L} + Y_R \sqrt{\rho_R}}{\sqrt{\rho_L} + \sqrt{\rho_R}}, \qquad (4.27)$$

where $\hat{\gamma} = \gamma(\hat{q})$ and

$$\hat{X} = \frac{C_{v_1} C_{c_2}(\gamma_1 - \gamma_2)\hat{T}}{\hat{Y}C_{v_1} + (1 - \hat{Y})C_{v_2}} \qquad (4.28)$$

with

$$\hat{T} = \frac{T_L \sqrt{\rho_L} + T_R \sqrt{\rho_R}}{\sqrt{\rho_L} + \sqrt{\rho_R}}. \qquad (4.29)$$

The matrix $\hat{\mathbf{A}}$ defined by the above is then diagonalizable: its eigenvalues are $\hat{u} - \hat{c}$, $\hat{u}$, $\hat{u} + \hat{c}$, where $\hat{c}^2 = (\hat{\gamma} - 1)$ $(\hat{H} - \hat{u}^2/2)$, and its eigenvectors are given by expressions which are analogous to Eqs. (4.16)–(4.17). This expression has an analogue in our immiscible case. We describe this and our numerical method in the next section.

V. APPROXIMATION TO EQUATIONS OF MOTION

The system is discretized in space by a second-order TVD (or ENO) scheme and in time by a two-stage TVD Runge–Kutta scheme which is second-order accurate in time. We follow the approach described in [64] and stop at the second-order accurate level.

Briefly, we set up a semi-discrete method of lines approximation to the system written as

$$\mathbf{q}_t = \bar{L}(\mathbf{q}).\tag{5.1}$$

The TVD operator $L(\mathbf{q})$ approximates $\bar{L}(\mathbf{q})$ to second order,

$$\bar{L}(\mathbf{q}) = L(\mathbf{q}) + O(h^2)\tag{5.2}$$

for smooth $\mathbf{q}$, where h is the maximum mesh size. The Euler forward version

$$\mathbf{q}^{n+1} = \mathbf{q}^n + \Delta t\, L(\mathbf{q}^n)\tag{5.3}$$

is assumed to be total variation stable for

$$\Delta t \leqslant \tfrac{2}{3}\max(|u|/\Delta x + |v|/\Delta y + c\sqrt{1/\Delta x^2 + 1/\Delta y^2})^{-1}\tag{5.4}$$

(a discussion of this criterion appears in [64] and some of the references described therein).

A second-order TVD Runge–Kutta time discretization is just Heun's method,

$$\begin{aligned}\mathbf{q}^* &= \mathbf{q}^n + \Delta t\, L[\mathbf{q}^n]\\ \mathbf{q}^{n+1} &= \frac{1}{2}(\mathbf{q}^n + \mathbf{q}^*) + \frac{\Delta t}{2} L[\mathbf{q}^*]\end{aligned}\tag{5.5}$$

which is stable under the same CFL condition as the Euler forward version.

Next we describe the space discretization

$$L(\mathbf{q}) = L^x[\mathbf{q}] + L^y[\mathbf{q}] + H(\mathbf{q}).\tag{5.6}$$

Here, of course, L^x approximates $-F_x$, L_y approximates $-G_y$, and $H(\mathbf{q})$ is the exact value of $H(\mathbf{q})$ at the grid point. The most intricate part of the discretization involves L^x and L^y. We describe L^x here; L^y is defined analogously.

L^x will be a conservation form finite difference scheme

$$L^x = -\frac{1}{\Delta x}(\hat{f}_{j+1/2} - \hat{f}_{j-1/2}),\tag{5.7}$$

where the numerical flux, $\hat{f}_{j+1/2}$ is a second-order-accurate approximation to $F(\mathbf{q})$ at the end point of a cell

$$I_j = \{x \mid x_{j-1/2} \leqslant x \leqslant x_{j+1/2}\}\tag{5.8}$$

and $\mathbf{q}(x_j, t^n)$ is obtained at all time levels, for $x_j = \frac{1}{2}(x_{j+1/2} + x_{j-1/2})$, the cell center.

First we determine the Roe decomposition. The average Jacobian $A_{j+1/2}$ for our system is analogous to the two component flow Roe matrix in [35]:

$$\mathbf{A}_{LR} = \left\{\begin{array}{c} 0 \\ 1/2(\hat{\gamma}-1)(\hat{u}^2 + \hat{v}^2) - \hat{u}^2 - \hat{\psi}\hat{X} \\ -\hat{u}\hat{v} \\ -\hat{u}[\hat{H} - 1/2(\hat{\gamma}-1)(\hat{u}^2 + \hat{v}^2) + \hat{\psi}\hat{X}] \\ -\hat{\psi}\hat{u} \end{array}\right.$$

$$\left.\begin{array}{cccc} 1 & 0 & 0 & 0 \\ (3-\hat{\gamma})\hat{u} & -(\hat{\gamma}-1)\hat{v} & (\hat{\gamma}-1) & \hat{X} \\ \hat{v} & \hat{u} & 0 & 0 \\ \hat{H} - (\hat{\gamma}-1)\hat{u}^2 & -(\hat{\gamma}-1)\hat{u}\hat{v} & \hat{\gamma}\hat{u} & \hat{u}\hat{X} \\ \hat{\psi} & 0 & 0 & \hat{u} \end{array}\right\}.\tag{5.9}$$

The averaged states are defined by

$$\hat{\rho} = \sqrt{\rho_L}\,\sqrt{\rho_R}\tag{5.10}$$

$$\hat{u} = \frac{\sqrt{\rho_L}\,u_L\,\sqrt{\rho_R}\,u_R}{\sqrt{\rho_L} + \sqrt{\rho_R}}\tag{5.11}$$

with $\hat{v}$, $\hat{H}$, and $\hat{\psi}$ defined in the same way as $\hat{u}$. The condition that remains is

$$\hat{X} = \frac{(P_R - P_L) - (\hat{\gamma}-1)[P_R/(\gamma_R - 1) - P_L/(\gamma_L - 1)]}{\hat{P}(\psi_R - \psi_L)}.\tag{5.12}$$

Note that $\hat{p} = \hat{\rho}\hat{c}^2/\hat{\gamma} = \hat{\rho}(\hat{\gamma}-1)(\hat{H} - 1/2(\hat{u}^2 + \hat{v}^2))/\hat{\gamma}$. Let $\Delta a = a_R - a_L$ for some quantity a, and define a_0 by $a_0 = \Delta p/(p\,\Delta\psi)$ and a_1 by $a_1 = \Delta(p/(\gamma - 1))/(p\,\Delta\psi)$. Then Eq. (5.11) becomes

$$\frac{d(\hat{\gamma}-1)}{d\hat{\psi}} = a_0(\hat{\gamma}-1) - a_1(\hat{\gamma}-1)^2.\tag{5.13}$$

It is not possible to find a function $\gamma(\psi)$ satisfying Eq. (5.13) with boundary conditions $\gamma(\psi_L) = \psi_L$. Therefore we choose

$$\gamma(\psi) = \frac{(\psi - \psi_L)\gamma_R + (\psi_R - \psi)\gamma_L}{\psi_R - \psi_L}\tag{5.14}$$

and let $\hat{\gamma} = \gamma(\hat{\psi})$. Now the condition given in Eq. (4.22) is not satisfied consistently, but it can be used to compute $\hat{\gamma}(\psi)$ or $\hat{X}$. Thus, we have obtained a matrix $\hat{A}$ which is almost equal to $A(\hat{w})$, except for $\hat{X}$. The right eigenvector of $\hat{A}$ are the columns of

$$\mathbf{T} = \left\{\begin{array}{ccccc} 1 & 1 & 0 & 0 & 1 \\ \hat{u} - \hat{c} & \hat{u} & 0 & 0 & \hat{u} + \hat{c} \\ \hat{v} & \hat{v} & 1 & 0 & v\hat{a} \\ \hat{H} - \hat{u}\hat{c} & 1/2(\hat{u}^2 + \hat{v}^2) & \hat{v} & -\hat{X}/(\hat{\gamma}-1) & \hat{H} + \hat{u}\hat{c} \\ \hat{\psi} & \hat{\psi} & 0 & 1 & \hat{\psi} \end{array}\right\}, \tag{5.15}$$

whereas the left eigenvectors l^k can be taken as the rows of T^{-1}. The left eigenvectors obey the relations:

$$l^2 = (1 - 1/2(\hat{\gamma} - 1)(\hat{u}^2 + \hat{v}^2)/\hat{c}^2$$
$$+ \hat{\psi}\hat{X}/\hat{c}^2, (\hat{\gamma} - 1)\hat{u}/\hat{c}^2, -(\hat{\gamma} - 1)/\hat{c}^2, -\hat{X}/\hat{c}^2)$$

$$l^3 = (-\hat{v}, 0, 1, 0, 0)$$
$$l^4 = (-\hat{\psi}, 0, 0, 0, 1)$$ (5.16)

$$l^1 + l^5 = (1, 0, 0, 0, 0) - l^2$$

$$l^1 - l^5 = (\hat{u}/\hat{c}, -1/\hat{c}, 0, 0, 0).$$

The eigenvalues are the diagonal elements of

$$\Lambda = \text{diag}(\hat{u} - \hat{c}, \hat{u}, \hat{u}, \hat{u}, \hat{u} + \hat{c}).$$ (5.17)

The Roe-type matrix above has terms which are almost infinite (that is, behave like $1/\Delta x$), because of Eq. (5.13). This mirrors the delta function occurring in the Jacobian when ψ changes sign. In spite of this, no stability problems were found in our calculations below.

ALGORITHM (TVD–Roe). Given the states $\mathbf{q}_j = \mathbf{q}(x_j)$, where the x_j are grid points, we compute the fluxes $f_j = f(\mathbf{q}_j)$. To determine the numerical flux $\hat{f}_{j+1/2}$, we transform to characteristic (Riemann invariant-like) variables.

We denote the left eigenvectors (computed in Eq. (5.15)), the right eigenvectors, and the eigenvalues of $\mathbf{A}_{j+1/2} = \mathbf{A}_{LR}$ (see Eq. (5.15) (left state $\mathbf{q}_l = \mathbf{q}_j$, right state $\mathbf{q}_r = \mathbf{q}_{j+1}$) by $l_{j+1/2}^{(v)}$, $r_{j+1/2}^{(v)}$, $\lambda_{j+1/2}^{(v)}$, $v = 1, 2, 3, 4, 5$. Computation shows that

$$\lambda_{j+1/2}^{(1)} = u_{j+1/2} - c_{j+1/2}$$ (5.18)

$$\lambda_{j+1/2}^{(2)} = \lambda_{j+1/2}^{(3)} = \lambda_{j+1/2}^{(4)} = u_{j+1/2}$$ (5.19)

$$\lambda_{j+1/2}^{(5)} = u_{j+1/2} - c_{j+1/2}.$$ (5.20)

Also,

$$l_{j+1/2}^{(v)} \cdot r_{j+1/2}^{(v)} = \delta_{v\mu} = \begin{cases} 1 & \text{if } v = \mu \\ 0 & \text{if } v \neq \mu \end{cases}.$$ (5.21)

We may decompose

$$f_k = \sum_{v=1}^{v=5} r_{j+1/2}^{(v)} \cdot G_k^{(v)}, \qquad k = j - 1, ..., j + 2,$$ (5.22)

where

$$G_k^{(v)} = l_{j+1/2}^{(v)} \cdot f_k.$$ (5.23)

The next step is just second-order-accurate ENO integration on $G_k^{(v)}$, namely,

$$G_L^{(v)} = G_j^{(v)} + 1/2\Delta_j^{(v)}$$ (5.24)

$$G_R^{(v)} = G_{j+1}^{(v)} - 1/2\Delta_{j+1}^{(v)}.$$ (5.25)

If

$$a_j^{(v)} = G_j^{(v)} - G_{j-1}^{(v)}, \qquad b_j^{(v)} = G_{j+1}^{(v)} - G_j^{(v)},$$ (5.26)

then

$$\Delta_j^{(v)} = \begin{cases} a_j^{(v)} & \text{if } |a_j^{(v)}| \leq b_j^{(v)}| \\ b_j^{(v)} & \text{otherwise.} \end{cases}$$ (5.27)

Upwind differencing is now applied to the field

$$G_{j+1/2}^{(v)} = \begin{cases} G_L^{(v)} & \text{if } \lambda_{j+1/2}^{(v)} \geq 0 \\ G_R^{(v)} & \text{otherwise.} \end{cases}$$ (5.28)

Finally, we transform back by letting

$$\hat{f}_{j+1/2} = \sum_{v=1}^{5} r_{j+1/2}^{(v)} \cdot G_{j+1/2}^{(v)}.$$ (5.29)

This is a (slightly nonstandard) version of a second-order-accurate TVD Roe-based scheme, see [64]. As such, it is known to admit stationary expansion shocks. An entropy fix due to Harten [24] is obtained through

$$G_{j+1/2} = 1/2[G_L^{(v)} + G_R^{(v)} - g(\lambda_{j+1/2}^{(v)})(G_R^{(v)} - G_L^{(v)})],$$ (5.30)

where

$$g(x) = \begin{cases} \text{sign}(x) & \text{if } |x| \geq \varepsilon_f \\ \dfrac{x^2 + \varepsilon_f^2}{2x\varepsilon_f} & \text{if } \varepsilon_f^2 < |x| < \varepsilon_f \\ \dfrac{\varepsilon_f^4 + \varepsilon_f^2}{2\varepsilon_f^3} & \text{if } |x| < \varepsilon_f^2. \end{cases}$$ (5.31)

We choose $\varepsilon_f = 0.1c_{j+1/2}$. This entropy fix suppresses unphysical expansion shocks and is only applied for the characteristic field $v = 1$ if $(u - c)_j < 0 < (u - c)_{j+1}$ and for field $v = 5$ if $(u + c)_j < 0 < (u + c)_{j+1}$.

We have now created a numerical flux function in all cases, including those for which $\gamma_j \neq \gamma_{j+1}$, for which the interface lies between x_j and x_{j+1} (recall Eq. (5.14)).

Finally, we consider the case for computations where the equation for ψ is not in conservation form. The term $u\psi_x$ is approximated via

$$(\Delta x) u\psi_x \approx u_j^+ ([\psi_j + 1/2(\Delta\psi)_j] - [\psi_{j-1} + 1/2(\Delta\psi)_{j-1}])$$
$$+ u_j^- ([\psi_{j+1} - 1/2(\Delta\psi)_{j+1}] - [\psi_j - 1/2(\Delta\psi)_j]),$$
(5.32a)

where

$$u_j^+ = \max(u_j, 0), \qquad u_j^- = \min(u_j, 0), \qquad (5.32b)$$

and

$(\Delta\psi)_j$ = smaller in absolute value of

$$(\psi_{j+1} - \psi_j, \psi_j - \psi_{j-1}). \qquad (5.32c)$$

This differencing corresponds to a second-order-accurate, stable, nonoscillatory approximation to the linear Hamilton–Jacobi equation $\psi_t = -u(x, t)\psi_x$, where u is a given function, see [47]. The other term $v\psi_y$ is approximated analogously.

The spatial discretization of the remaining four equations is as described above, and the time discretization is just Heun's method, one again. We repeat, the extension to two space dimensions comes from approximations to $L^x(q)$ and $L^y(q)$ separately in the one-dimensional fashion described in Eqs. (5.7)–(5.32), then using the Runga–Kutta time discretization shown in Eq. (5.5).

VI. RESULTS

A. Rayleigh–Taylor Instability

The numerical experiments were performed on a rectangular domain with walls on the lower and upper sides, and periodic boundaries in the horizontal direction. Gravity acts in the upward direction. The horizontal size of the domain is chosen as the unit length. An initial sine perturbation has a wavelength λ of the same size. As initial conditions, we use the solution of the linearized equations given in [21]. This solution refers to the air–air case. The relevant parameters are the initial density ratio $D = \rho_b/\rho_a$ and $M^2 = g\lambda^2/c_b^2$. The subscript a refers to the gas just above the interface, the subscript b to gas just below the interface. The sound speed just below the interface c_b is set to 1, as is the density ($c_b = 1$, $\rho_b = 1$). The constant of gravity follows from M^2. The adiabatic exponent $\gamma_a = \gamma_b = 1.40$.

Figure 1 shows contours of ψ at values of $-1/32$, 0, and $1/32$, for times 0, 1, ..., 6. The grids have size 64×128 and 192×384, respectively. Symmetry is forced: the computations have been carried out on a grid with half the size in the horizontal direction. Thus, the grids used are in fact 32×128 and 96×384, respectively. The initial density ratio D is 2, the amplitude of the initial perturbation is 0.015, and $M^2 = 0.5$.

In Fig. 1a, we see that a small sinusoidal perturbation grows into the expected mushroomshaped object and develops side rolls. However, tripling the mesh size, shown in Fig. 1b, does not produce a refined picture. Instead, pronounced oscillations develop and smaller rolls appear on the surface of the basic structure. This suggests that the

solution does not converge under refinement. As a test, we compute the relative error in ψ defined by

$$E_h^{2h}(\psi) = \|\psi^{2h} - I_h^{2h}\psi_h\|, \qquad (6.1)$$

where the superscript h denotes the cell size of the uniform grid and $2h$ denotes the grid size after coarsening. In order to compare the two, we apply the restriction operator I_h^{2h} to the solution of the fine mesh and volume average to produce values for comparison with the coarse mesh solution. The initial data are represented with second-order accuracy

TABLE Ia

Relative Error $E_h^{2h}(\psi)$ Measured in the l_1 Norm, as a Function of Grid Size and Viscosity μ at Times 0, 2, 4, and 6, for the Rayleigh–Taylor Problem

$(2h)^{-1}, h^{-1}$	Time	$\mu = 0$	5×10^{-4}	1×10^{-3}	5×10^{-3}
32, 64	0	1.15−5	1.15−5	1.15−5	1.15−5
	2	4.03−4	3.22−4	5.13−4	3.46−4
	4	7.37−3	4.79−3	3.70−3	1.08−3
	6	2.79−2	2.47−2	2.02−2	5.67−3
48. 96	0	5.11−6	5.11−6	5.11−6	5.11−6
	2	2.79−4	1.80−4	2.46−4	1.62−4
	4	6.40−3	3.42−3	2.27−3	5.48−4
	6	2.88−2	1.80−2	1.39−2	3.19−3
64, 128	0	2.87−6	2.87−6	2.87−6	2.87−6
	2	2.34−4	1.21−4	1.55−4	9.71−5
	4	5.90−3	2.58−3	1.58−3	3.46−4
	6	3.57−2	1.22−2	9.59−3	2.10−3
96, 192	0	1.28−6	1.28−6	1.28−6	1.28−6
	2	1.71−4	6.85−5	8.04−5	5.05−5
	4	5.71−3	1.52−3	8.42−4	1.92−4
	6	6.20−2	6.64−3	5.14−3	1.16−3

TABLE Ib

Order of Accuracy, Estimated from the Relative Error in ψ Measured in the l_1 and l_∞ Norms, as a Function of the Viscosity μ at Various Times, for the Rayleigh–Taylor Problem

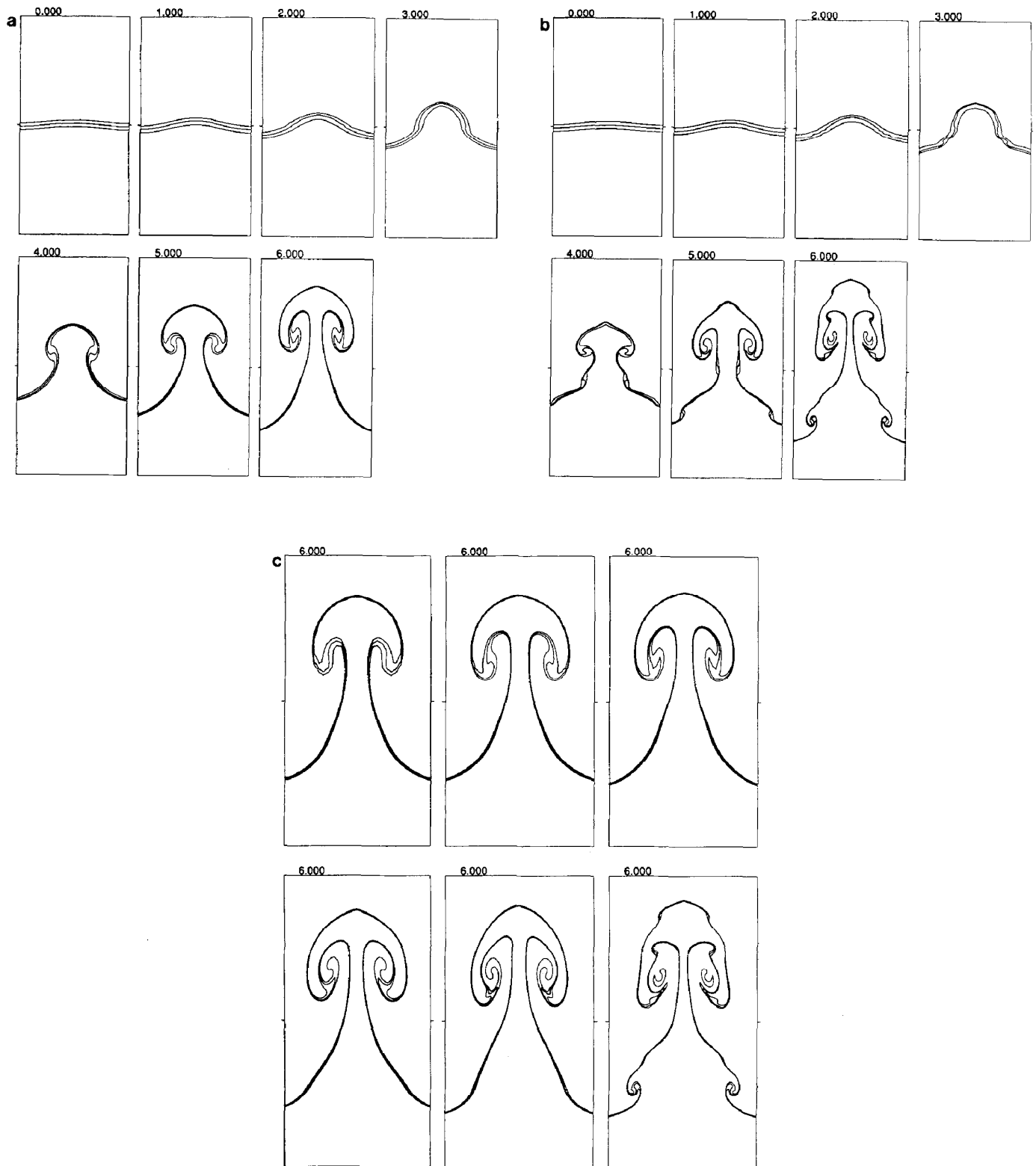| μ	Norm	$t = 0$	$t = 2$	$t = 4$	$t = 6$
0	l_1	2.00	1.04	0.16	−0.93
	l_∞	1.95	0.01	−0.41	−0.81
5×10^{-4}	l_1	2.00	1.62	1.22	1.42
	l_∞	1.95	0.83	0.98	0.78
1×10^{-3}	l_1	2.00	1.63	1.46	1.43
	l_∞	1.95	0.78	1.29	0.97
5×10^{-3}	l_1	2.00	1.67	1.51	1.46
	l_∞	1.95	0.61	0.84	1.32

FIG. 1. (a) Contours of ψ at values of $-\frac{1}{32}$, 0, and $\frac{1}{32}$, for a 64 × 128 grid. The computation has been carried out on a 32 × 128 grid, with forced symmetry. (b) As Fig. 1a, but for a 192 × 384 grid. (c) Grid refinement sequence at time 6. We have $h^{-1} = 32$, 48, 64, 96, 128, and 192, from left to right, top to bottom.
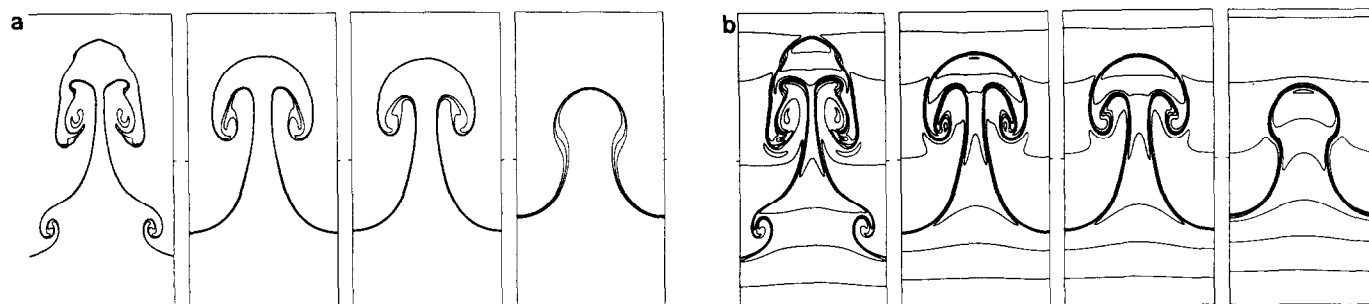
FIG. 2. (a) Contours of ψ at values of $-\frac{1}{32}$, 0, and $\frac{1}{32}$, for the computations described in Table I at time 6. The viscosity μ has values 0, 5×10^{-4}, 1×10^{-3}, 5×10^{-3}, and increases from left to right. (b) As Fig. 2a, but now the density is plotted. Contours are 0.1 apart.

$E_h^{2h} = O(h^2)$. For short time, the error decreases as h is refined. However, for larger times $T > 4$, the error increases as the mesh is refined. In Tables I, we show these results for the inviscid ($\mu = 0$) case.

Because the problem is physically unstable, our solution does not converge under grid refinement. To obtain a converged solution, we add physical viscosity. The Navier–Stokes equations without heat conduction are used. Following Stokes hypothesis, the second coefficient of viscosity $\lambda = -\frac{2}{3}\mu$. The first coefficient of viscosity μ is chosen to be constant. The spatial discretization is based on the usual central differences. The timestep is chosen as

$$\Delta t = \left(\frac{\lambda_1}{\text{CFL}_1} + \frac{\lambda_2}{\text{CFL}_2}\right)^{-1}, \tag{6.2}$$

where

$$\lambda_1 = \max(|u| + |v| + c\sqrt{2})/h,$$

$$\lambda_2 = \frac{14}{3}\frac{\mu}{h^2}\frac{1}{\min(\rho)}. \tag{6.3}$$

Here the maximum and minimum are computed over the grid. We use $\text{CFL}_1 = \frac{2}{3}$ and $\text{CFL}_2 = 1$.

The addition of physical viscosity stablizes the problem. We performed runs with grid sizes of 32, 48, 64, 96, 128, and 192 mesh points across the horizontal width, with twice as many points in the vertical direction. The results indicate that convergence improves with the larger values of viscosity μ. Table Ia shows the relative errors E_h^{2h} in ψ, computed from a grid refinement sequence with h^{-1} equal to 32,
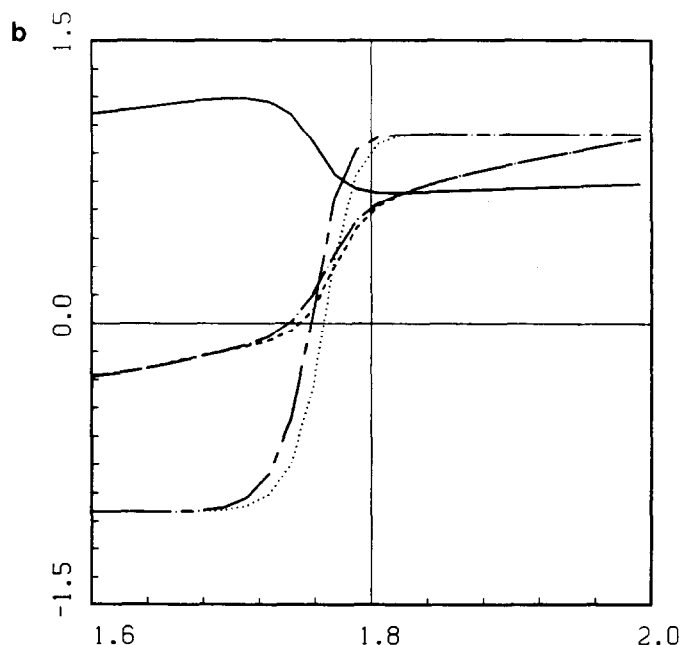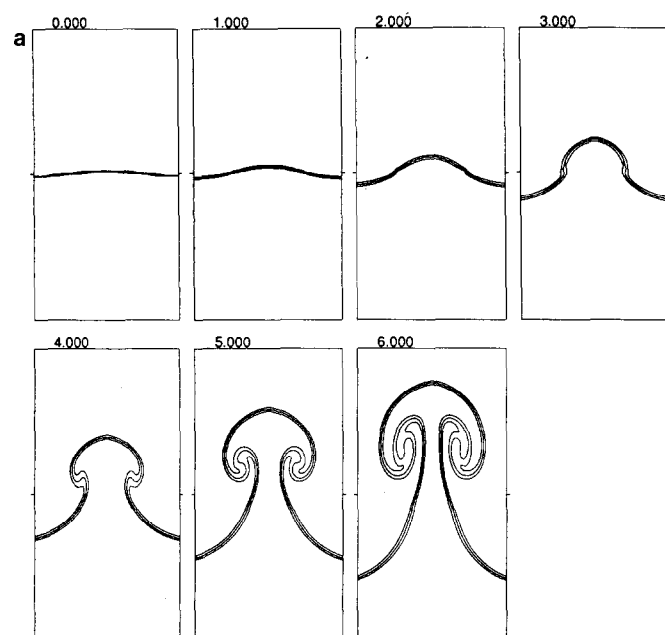

FIG. 3. (a) Contours of the color function at -0.5, 0.0, and 0.5 for a 64×128 grid. The computation has been carried out on a 32×128 grid, with forced symmetry. (b) Vertical cross section halfway Fig. 3a at time 6. Shown are ρ (drawn line), ψ (dashed), and the color function (dots). Also shown are runs for non-conservative differencing: ψ = chain-dot, color function = chain-dash.
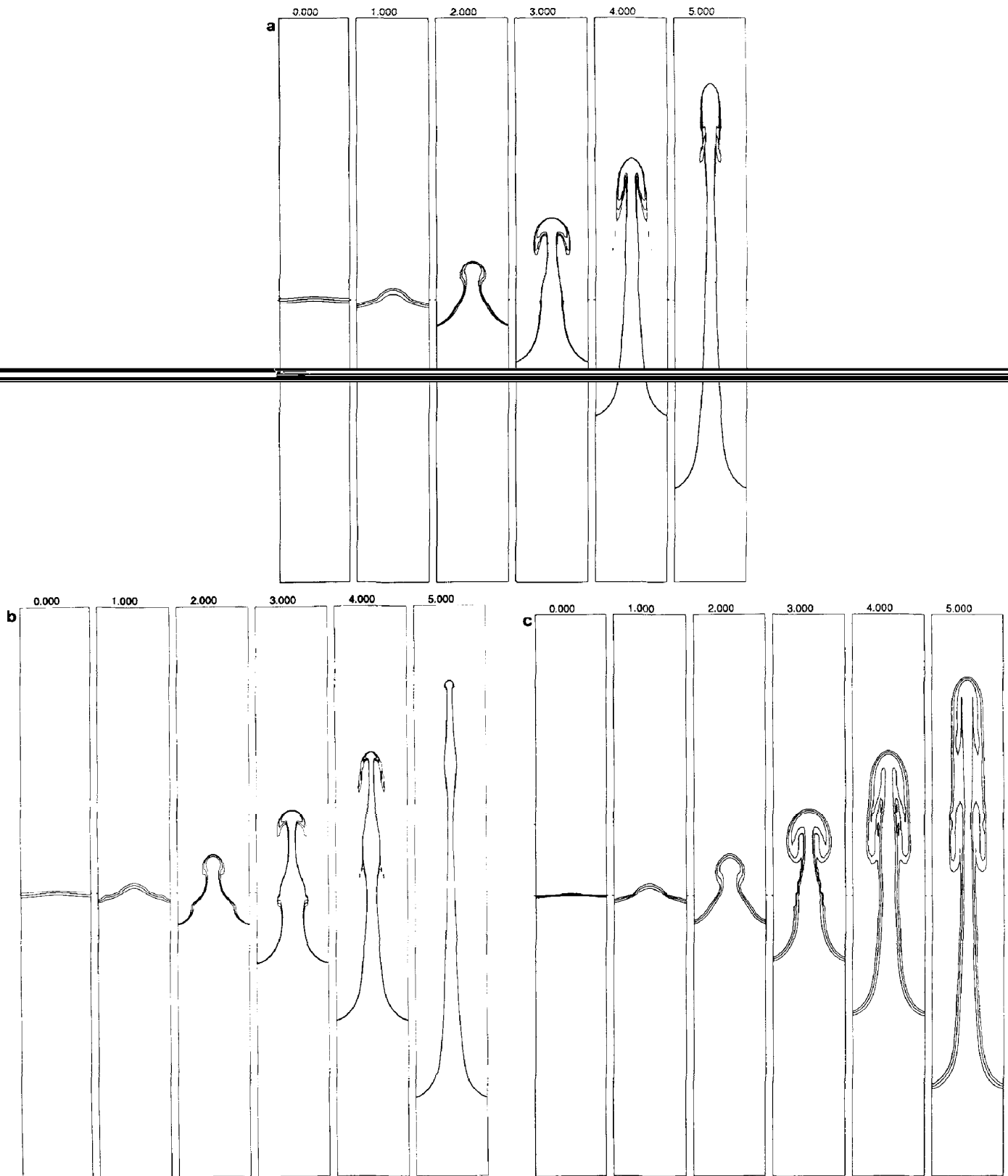
FIG. 4. (a) Contours of ψ at values of $-\frac{1}{32}$, 0, and $\frac{1}{32}$, for a 32 × 256 grid, in the helium–air case. (b) Same parameters and initialization with non-conservative differencing: ψ = chain-dot, color function = chain-dash. (c) As Fig. 4a, but now ψ has been initialized as -1 and $+1$, representing a color function. Contours are at -0.5, 0.0, and 0.5. (d) As Fig. 4a, but using the concentration Y to determine the effective value of γ. Contours are drawn at 0.25, 0.50, and 0.75. (e) The (passive) function ψ at values $-\frac{1}{32}$, 0, and $\frac{1}{32}$, for the same computation as in Fig. 4d.
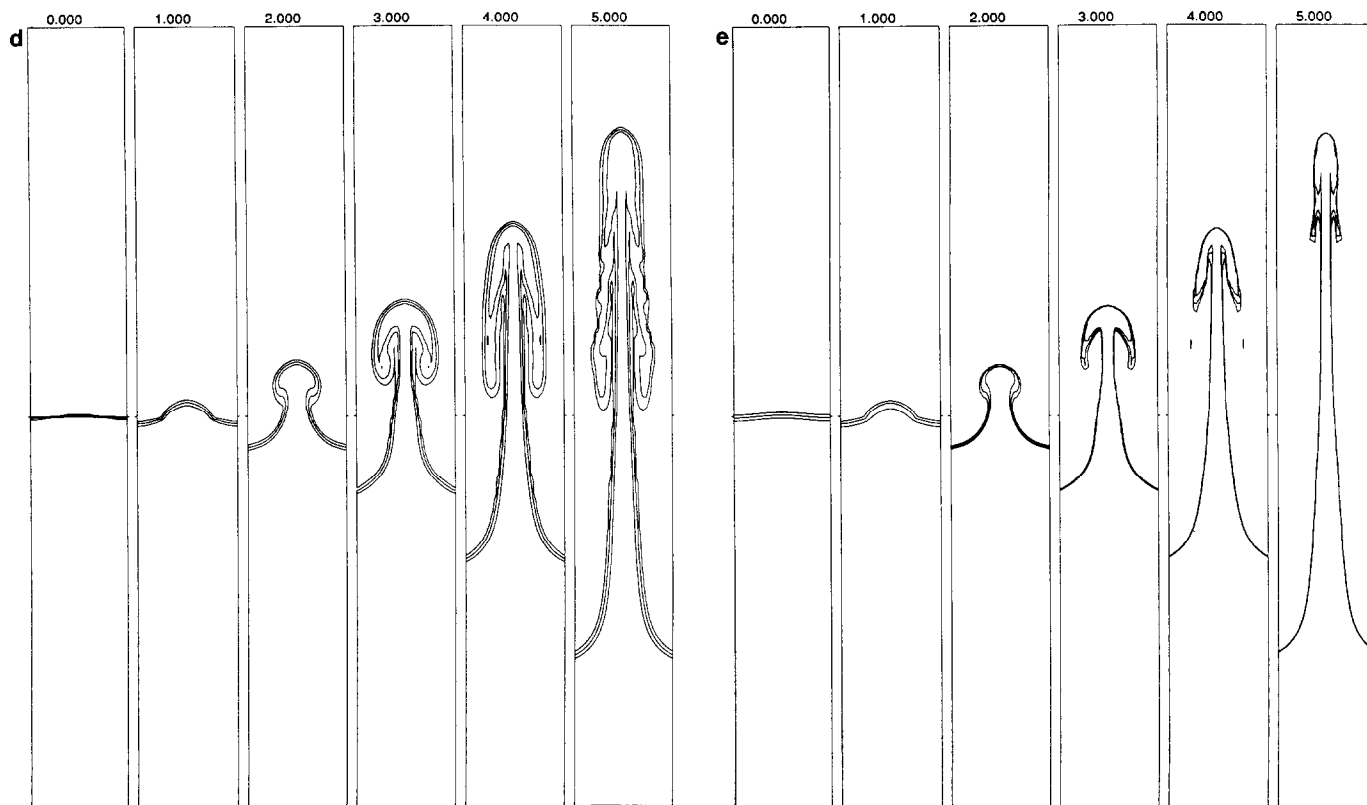
FIG. 4—*Continued*

48, 64, 96, 128, and 192. The number of points in the vertical direction is twice that amount. Once again, symmetry is enforced so that only half as many points are used in the horizontal direction, producing a symmetric portrait.

Table Ib shows the order of accuracy p, estimated by a weighted least-squares fit to $\log E_h^{2h}(\psi) = b_0 + p \log h$, using h^{-2} as weight. The grids used have 64, 96, 128, 192, 256, and 384 points in the vertical direction and half that number in the horizontal direction (actually $\frac{1}{4}$, with the forced symmetry). This provides four data points for each least-squares fit. It is clear that without viscosity, the error increases under grid refinement. In the viscous case, convergence improves with larger values of the viscosity μ.

Figure 2a shows ψ at time 6, for various choices of μ; Fig. 2b shows the density ρ for the same parameters. Since there is no feedback mechanism from the front to the fluid, the density of the fluid is a good indicator of the front position. Comparison of the two figures reveals the cosmetic character of ψ.

The above calculations consider a conservative differencing of ψ, initialized as the signed distance to the initial front, as given in Eq. (2.2). We now consider alternatives to this approach. To begin, other researchers have tracked fronts by following the evolution of a "color" function, which is -1 on one side of the front and $+1$ on the other. A sophisticated variant of this idea using a version

of SLIC to gain subcell resolution was employed in [13] to performed detailed calculations and comparison with experiment of a shock wave hitting a gas interface. We may incorporate a color function into our code by initializing ψ to ± 1. Figure 3a displays the result of a computation identical to the one in Fig. 1a, but using the color function instead of ψ. Comparison shows that the color function suggests a faster evolution of the instability than ψ. This is highlighted in Fig. 3b, which shows part of a vertical section through the middle of Fig. 3a.

Next, we consider non-conservative differencing, as discussed in Section III.A. Here, the standard four-component hyperbolic system is solved, and those velocities are then used in a second-order-accurate upwind fashion to advect ψ using Eq. (3.7), as described in the text. In Fig. 3b, we compare the results of conservative and non-conservative differencing of both the initialized distance function for ψ and the color function. Our results here seem to indicate that the non-conservative differencing of ψ using the level set initial distance function is most desirable (see the Appendix).

The motion of the front becomes significantly more complicated when we allow feedback between the front location and the fluid mechanics. Consider an air–helium boundary. Here, the bottom gas is air with $\gamma_b = 1.40$ (air), and the top gas is helium with $\gamma_t = 1.63$ (He). As the initial condition we again use the linearized solution. Using the molecular
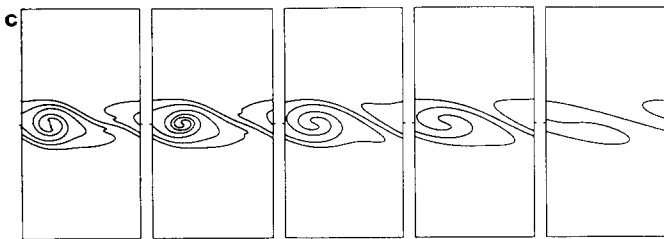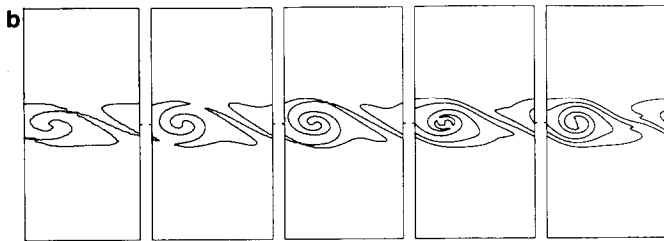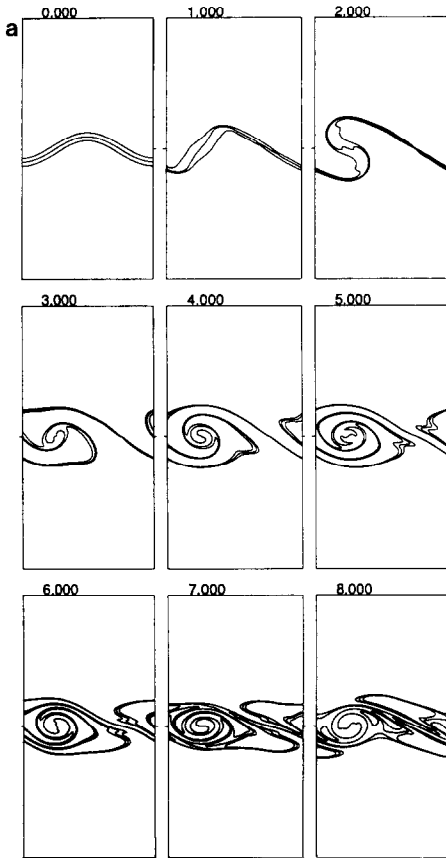
weights $\mu_b = 29.0$ and $\mu_a = 4.0$, we set $c_b = 1$ and $\rho_b = 1$ and find a density ratio by assuming constant temperature and pressure across the interface. This implies that the density ratio $D = \rho_b/\rho_a = \mu_b/\mu_a$ and that $c_a^2 = c_b^2(\gamma_a/\gamma_b)D$.

In Fig. 4a, we model this problem using conservative differencing of the level set/gas dynamic five-component hyperbolic system and the original distance function ψ initialization. Calculations are performed on a 32 × 256 grid, again with the forced symmetry in the horizontal direction requiring half as many horizontal grid points. The small initial bubble grows upwards into a long plume. We show contours of ψ at $-\frac{1}{32}$, 0, $\frac{1}{32}$. In Fig. 4b, we perform the same calculation using non-conservative differencing for ψ. We believe this to be the more accurate calculation, since we do not decode ψ using a discontinuous density. For comparison, in Fig. 4c we show results using ψ initialized as a piecewise constant color function, namely -1 on one side and $+1$ on the other side of the interface. Finally, the results of a different computation with the effective adiabatic exponent based on the concentration Y, as in [35], is shown in Fig. 4d. We have included ψ in this computation as well, as a passive scalar. Contours of ψ are presented in Fig. 4e.

Computations based on the concentration Y model dif-

FIG. 5. (a) Kelvin–Helmholtz instability. Shown are contours of the (passive) function ψ at values $-\frac{1}{32}$, 0, and $\frac{1}{32}$. The grid has 128 × 256 points. (b) Grid refinement sequence at time 6, for $h^{-1} = 32, 48, 64, 96$, and 128. (c) Zero contours of ψ for the computations described in Table II at time 6. The viscosity μ has values $0, 1 \times 10^{-4}, 5 \times 10^{-4}, 1 \times 10^{-3}, 5 \times 10^{-3}$ and increases from left to right.
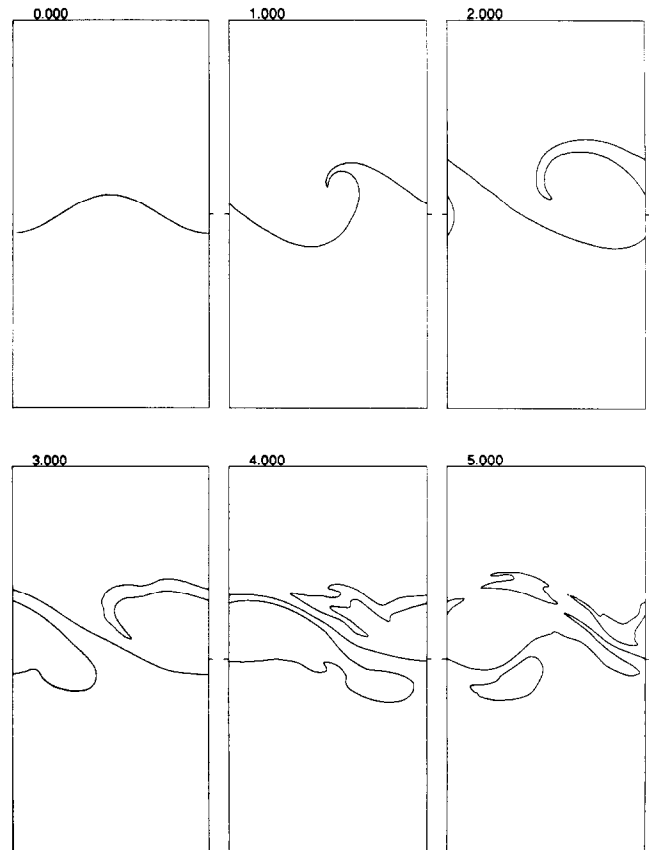

FIG. 6. Kelvin–Helmholtz instability for air (above the interface) and helium (below the interface), on a 128 × 256 grid.

ferent physics. Still, the plot of the passive ψ corresponds fairly closely to the one in Fig. 4a. A comparison between Figs. 4c and 4d shows that it is not so easy to determine the position of the (smeared) front from the concentration. This smearing might be considerably reduced with the help of artificial compression as described in [64]. Even better would be a two-dimensional version of sub-cell resolution [25].

B. Kelvin–Helmholtz Instability

Next, we perform calculations of the Kelvin–Helmholtz instability. As initial conditions, we take constant pressure

TABLE IIa

Relative Error $E_h^{2h}(\psi)$ Measured in the l_1 Norm, as a Function of Grid size and Viscosity μ at Times 0, 2, 4, and 6, for the Kelvin–Helmholtz Problem

(2h, h)	Time	$\mu = 0$	1×10^{-4}	5×10^{-4}	1×10^{-3}	5×10^{-3}
32, 64	0	3.94−5	3.94−5	3.94−5	3.94−5	3.94−5
	2	6.64−3	6.47−3	5.45−3	4.73−3	2.79−3
	4	1.28−2	1.20−2	9.06−3	8.20−3	4.44−3
	6	1.64−2	1.64−2	1.25 2	1.04 2	5.33 3
	8	1.04−2	1.21−2	1.36−2	1.14−2	5.55−3
48, 96	0	1.76−5	1.76−5	1.76−5	1.76−5	1.76−5
	2	5.64−3	5.18−3	3.71−3	2.89−3	1.57−3
	4	1.34−2	1.24−2	7.47−3	5.09−3	2.54−3
	6	1.77−2	1.69−2	1.19−2	8.07−3	3.20−3
	8	1.86−2	1.62−2	9.86−3	9.27−3	3.42−3
64, 128	0	9.93−6	9.93−6	9.93−6	9.93−6	9.93−6
	2	5.11−3	4.33−3	2.68−3	1.95−3	1.02−3
	4	1.29−2	1.13−2	6.16−3	3.69−3	1.69−3
	6	1.89−2	1.74−2	1.03−2	6.48−3	2.19−3
	8	1.85−2	1.82−2	8.61−3	8.06−3	2.39−3

TABLE IIb

Order of Accuracy, Estimated from the Relative Error in ψ Measured in the l_1 and l_∞ Norms, as a Funcion of the Viscosity μ at Various Times, for the Kelvin–Helmholtz Instability

μ	Norm	$t = 0$	$t = 2$	$t = 4$	$t = 6$	$t = 8$
0	l_1	1.99	0.36	0.04	−0.21	−0.48
	l_∞	1.31	−0.19	−0.58	−1.02	−1.11
1×10^{-4}	l_1	1.99	0.60	0.18	−0.08	−0.51
	l_∞	1.31	0.02	−0.51	−0.90	−1.33
5×10^{-4}	l_1	1.99	1.07	0.60	0.36	0.58
	l_∞	1.13	0.81	0.46	−0.07	0.33
1×10^{-3}	l_1	1.99	1.31	1.14	0.72	0.49
	l_∞	1.13	1.24	0.92	0.29	0.18
5×10^{-3}	l_1	1.99	1.47	1.41	1.30	1.23
	l_∞	1.31	1.00	1.60	1.00	0.82

and temperature abvove and below the interface, with zero vertical velocity. The initial shape is a sine perturbation. Above the interface, the gas moves towards the left with velocity $u = -u_0$; below the interface, the horizontal velocity is $u = u_0$. For the air–air case, we set the density and the sound speed to 1 everywhere. Again we have periodic boundaries in the horizontal direction and walls at the bottom and top. Gravity is not included.

In Fig. 5a, we show the evolution of an initial perturbation with amplitude $a = 0.1$ and $u_0 = 0.25$. We use a 128×256 grid. We study an air–air interaction, so that the level function ψ is passively advected. We plot values of ψ at $-\frac{1}{32}, 0, \frac{1}{32}$. The results show the rollup of a vortex structure as it progresses through several turns. The small oscillations in the shape seem to indicate, once again, that we will not obtain a converged solution because of the physical instability of the underlying problem. We check this by values of h. In Fig. 5b, we show the results of a calculation on a 32×32, 64×64, 96×96, and 128×128 grid. The refinement in mesh size at fixed time suggests that the results are not stable.

Next, we add physical viscosity to the system. In Tables IIa and IIb, we show the error $E_h^{2h}(\psi)$ measured in the l_1 norm as a function of the grid size and viscosity μ at various times. The introduction of physical viscosity stablizes the problem. In Fig. 5c, we show zero contours of ψ at time $t = 6$, with viscosity $\mu = 0, 10^{-4}, 10^{-3}, 0, 5 \times 10^{-3}$ going from left to right. As expected, the introduction of physical viscosity slows the rollup.

Figure 6a shows the evolution for the air–helium case. The gas below the interface is helium. The initial conditions are $c_b = 1$, $\rho_b = 1$, $D = \rho_b/\rho_a = \mu_b/\mu_a$, $c_a^2 = c_b^2 D \gamma_a/\gamma_b$, $u = \pm u_0$, $v = 0$. This corresponds to constant initial pressure and temperature. We let $u_0 = 0.5$. The initial sine perturbation has an amplitude $a = 0.1$. The rollup can no longer be resolved after a time between 4 and 5.

DISCUSSION

In this paper, we have discussed the coupling of the level set formulation of interface motion to the equations of compressible gas dynamics. We have considered two approaches. In one approach, the level set equation is posed in non-conservative form and coupled to the four-component system. Alternatively, we have shown that a conservative version of the level set function ψ can be directly incorporated as a five-component system of hyperbolic conservation laws using standard shock technology. In both conservative and non-conservative settings, we have examined the distance function initialization of the level set function ψ and a degenerate initialization using the color function.

The efficiency of these various techniques depends on the particular problem under study. In the Rayleigh–Taylor problem we considered, the normal velocity varies continuously across the interface, unlike the density ρ, which undergoes a jump. In this case, the non-conservative formulation for ψ uses a smooth $\mathbf{u}$, and our results indicate that this approach is preferable to direct incorporation of ψ into the conservative system because of the discontinuity in $\rho\psi$. It seems reasonable to expect that for problems in which $\mathbf{u}$ jumps across the interface, the conservative approach will be preferable.

In the problems considered here, the front velocity does not depend on the geometry of the interface. All that is needed is a rough location of the front to determine the selected region for the gas constant. Thus, the ability of the Hamilton–Jacobi level set formulation to accurately calculate curvature and normal direction is untapped in this simple calculation. For such simple problems, the color function is an adequate initialization and leads to only slightly worse performance; however, we point that it is no cheaper than our original level set approach. Furthermore, in more sophisticated problems, see, for example, [62], the color function idea is insufficient and the full capabilities of the level set approach are utilized.

Finally, we have computed the solution to two complex physical phenomena. To what degree are these solutions accurate? First, we point out that in the zero viscosity limit, both of the problems are physically unstable. Our calculations in this case do not converge with respect to mesh refinement. We believe the following is a plausible scenario. Our schemes introduce artificial viscosity which decreases with decreasing mesh size. For a coarse enough mesh, the numerical viscosity stabilizes instabilities that occur in the zero viscosity limit, and the solution is smooth. This can be seen in the calculations with coarse grids given in Fig. 1c. As the mesh size is refined, and the artificial viscosity lessens, small physical instabilities are not suppressed and instead grow, as seen in the finer grid calculations of Fig. 1c.

In order to justify this hypothesis, we should be able to demonstrate that, given some amount of physical viscosity, we can compute on a fine enough grid so that the physical viscosity dominates the numerical viscosity or the results are unchanged with respect to further grid refinement. This is the experiment indicated in Tables I and II. On the basis of this, we believe that our technique is capturing a reasonable portrait of the solution in the viscous cases and reflects the physical instability of the problem in the zero viscous limit case. Of course, the particular unstable solution shown in the case $\mu = 0$ means little; only the gross features are of significance. In future work, we hope to use the notion of subcell resolution [25] together with the level set formulation to account more accurately for the small scale geometry of the front.

APPENDIX: COLOR VERSUS SMOOTH ψ

Consider the one-dimensional motion of a contact discontinuity. Let its speed be u_0. Then our system reduces to

$$\frac{\partial w}{\partial t} + u_0 \frac{\partial w}{\partial x} = 0, \qquad w = \begin{pmatrix} \rho \\ \rho\psi \end{pmatrix}. \tag{A1}$$

A first-order discretization of this system introduces numerical viscosity, which can be modeled by the equivalent equation

$$\frac{\partial w}{\partial t} + u_0 \frac{\partial w}{\partial x} = \varepsilon \frac{\partial^2 w}{\partial x^2}. \tag{A2}$$

Transforming to moving coordinates $x' = x - ut_0$, $t' = t$, produces the heat equation

$$w_t = \varepsilon w_{xx}, \tag{A3}$$

where the primes have been dropped. The solution is

$$w(x, t) = \int_{-\infty}^{\infty} K(x, y)\, w(y, 0)\, dy, \tag{A4}$$

where the kernel

$$K(x, y) = \frac{1}{2} (\pi \varepsilon t)^{-1/2} \exp\left(-\frac{(x-y)^2}{4\varepsilon t} \right). \tag{A5}$$

For initial data

$$w(x, 0) = \begin{cases} w_L & \text{if} \quad x < 0 \\ w_R & \text{if} \quad x > 0 \end{cases} \tag{A6}$$

the solution is

$$w(x, t) = w_L + (w_R - w_L)\, S(x, t),$$
$$S(x, t) = \frac{1}{2}\left[1 + \text{erf}\left(\frac{x}{2\sqrt{\varepsilon t}} \right) \right]. \tag{A7}$$

Let the color function be denoted by ψ^C, and the smooth version by ψ^S. Their initial data are

$$\psi^C = \begin{cases} -1, & x < 0 \\ 1, & x > 0 \end{cases} \tag{A8}$$

and

$$\psi^S(x, 0) = x, \tag{A9}$$

respectively. The initial density distribution is $\rho(x, 0) = \rho_L$

for negative and $\rho(x, 0) = \rho_R$ for positive x. The solutions are

$$\psi^C(x, t) = \frac{-\rho_L + (\rho_R + \rho_L) S(x, t)}{\rho_L + (\rho_R - \rho_L) S(x, t)} \qquad (A10)$$

and

$$\psi_S(x, t) = x + \frac{(\rho_R - \rho_L)}{\rho_L + (\rho_R - \rho_L) S(x, t)}$$

$$\times \left(\frac{\varepsilon t}{\pi}\right)^{1/2} \exp\left(-\frac{x^2}{4\varepsilon t}\right). \qquad (A11)$$

At $x = 0$, we find

$$\psi^S(0, t) = \frac{\rho_R - \rho_L}{\rho_R + \rho_L} \qquad (A12)$$

$$\psi^C(0, t) = \frac{\rho_R - \rho_L}{\rho_R + \rho_L}\left(\frac{4\varepsilon t}{\pi}\right)^{1/2}. \qquad (A13)$$

Let $A = (\rho_R - \rho_L)/(\rho_R + \rho_L)$. Then the point where $\psi^C(x, t) = 0$ is, for small A,

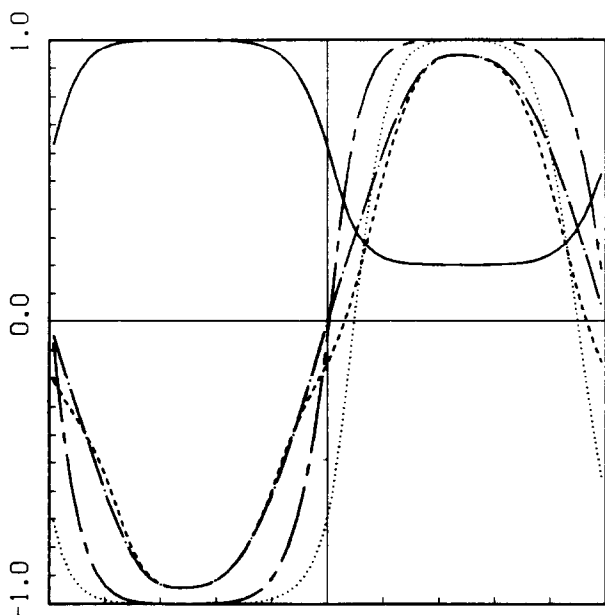$$x_0^C \approx A\sqrt{\pi\varepsilon t}, \qquad (A14)$$

FIG. 7. Propagation of two contact discontinuities on a periodic grid. The velocity $u_0 = 0.5$, the initial density is 1.0 or 0.2. Shown in the result at time 2, using second-order ENO/ROE. In the absence of numerical viscosity, the results would be identical to the initial data. The jumps in density (drawn line) occur at $x = 0$ and $x = 0.5$. The dashed line represents the function $\psi^{S(x,t)}$, initialized with $-\sin(2\pi x)$, whereas the dotted line displays the color function $\psi^{C(x,t)}$, initialized with -1 if $\rho = 1.0$ and $+1$ if $\rho = 0.2$. Also shown are the cases with non-conservative differencing.

whereas for the initially smooth $\psi^{S(x,t)}$ we find

$$x_0^C \approx A\sqrt{4\varepsilon t/\pi}. \qquad (A15)$$

Both are wrong; we should have $x_0 = 0$. The smooth function $\psi^{S(x,t)}$ is better than the color function $\psi^{C(x,t)}$ in monitoring the position of the front, but only by a factor $2/\pi = 0.64$.

Figure 7 illustrates what happens for the second-order ENO/ROE scheme. Two contacts are moving on a one-dimensional periodic grid. The density and color function are smeared, due to numerical viscosity. Although the numerical viscosity is smaller than for the first-order scheme, the zero-crossings of ψ^C and ψ^S appear to display the effect described above. Non-conservative differencing for both ψ^S and ψ^C are also shown. The non-conservative scheme for ψ^S seems to be the best choice.

REFERENCES

1. G. R. Baker, D. I. Meiron, and S. A. Orszag, Rayleigh–Taylor instability problems, *Physica D* 12, 19 (1984).

2. G. R. Baker, D. I. Meiron, and S. A. Orszag, *J. Fluid Mech.* 123, 477 (1982).

3. G. R. Baker, D. I. Meiron, and S. A. Orszag, *Phys. Fluids* 23 (8), 1485 (1980).

4. R. Bellman and R. H. Pennington, *Q. Appl. Math.* 12, 151 (1954).

5. B. B. Chakrabothy, *Phys. Fluids* 23 (3), 464 (1980).

6. B. B. Chakrabothy and J. Chandra, 19 (12), 1851 (1976).

7. J. W. Chalmers, S. W. Hodson, K. H. Winkler, P. Woodward, N. J. Zabusky, "Two-Dimensional Supersonic Flows," Vortex Motion: Proceedings of the IUTAM Symposium on Fundamental Aspects of Vortex Motion; *Fluid Dyn. Res.* 3, 392 (1988).

8. S. Chandrasekhar, *Hydrodynamic and Hydromagnetic Stability*, Oxford Univ. Press, London, 1961.

9. Y. G. Chen, Y. Giga, and S. Goto, preprint, (1989).

10. A. J. Chorin, *J. Fluid Mech.* 57, 785 (1973).

11. A. J. Chorin and P. S. Bernard, *J. Comput. Phys.* 13, 423 (1973).

12. R. L. Cole and R. S. Tankin, *Phys. Fluids* 16, 1810 (1973).

13. P. Colella, L. Henderson, and E. Puckett, in *Proceedings, 9th AIAA Computational Fluid Dynamics Conference, Buffalo, 1989*.

14. B. J. Daly, *Phys. Fluids* 10 (2), 297 (1967).

15. B. J. Daly, *Phys. Fluids* 12, 1340 (1969).

16. H. W. Emmons, C. T. Chang, and B. C. Watson, *J. Fluid Mech.* 7, 177 (1960).

17. L. C. Evans and J. Spruck, Motion of level sets ny mean curvature, preprint (1987).

18. P. T. Fink and W. K. Soh, *Proc. R. Soc. London A* 362, 195 (1978).

19. J. R. Freeman, M. J. Clauser, and S. L. Thomson, *Nucl. Fusion* 17, 223 (1977).

20. P. Garabedian, *Commun. Pure. Appl. Math.* 38, 609 (1985).

21. C. L. Gardner, J. Glimm, O. McBryan, R. Menikoff, D. H. Sharp, and Q. Zhang, *Phys. Fluids* 31, 447 (1988).

22. J. Glimm, O. McBryan, R. Menikoff, and D. H. Sharp, *SIAM J. Sci. Stat. Comput.* 7, 230 (1987).

23. F. H. Harlow and J. E. Welch, 8 (12), 2182 (1965).

24. A. Harten, **49**, 357 (1983).

25. A. Harten, **83**, 148 (1989).

26. C. W. Hirt, J. L. Cook, and T. D. Butler, *J. Comput. Phys.* **5**, 103 (1970).

27. D. Y. Hsieh, *Phys. Fluids* **22** (8), 1435 (1979).

28. J. W. Jacobs and I. Catton, *J. Fluid Mech.* **187**, 329 (1988).

31. R. Krasny, *J. Fluid Mech.* **167**, 65 (1986).

32. R. Krasny, *J. Fluid Mech.* **184**, 123 (1987).

33. R. Krasny, *J. Comput. Phys.* **65**, 292 (1986).

34. J. H. Krolik, *Phys. Fluids* **20** (3), 364 (1977).

35. B. Larrouturou and L. Fezoui, in *Non-linear Hyperbolic Problems* edited by Carasso, Charier, Hanouzet, and Joly, Lecture Notes in Mathematics (Springer-Verlag, Heidelberg, 1989).

36. K. J. Laskey, E. S. Oran, and J. P. Boris, "The Gradient Method for Interface Tracking," in *Numerical Simulation of Reactive Flow*, edited by E. S. Oran and J. P. Boris (Elsevier Science, New York, 1987).

37. D. J. Lewis, *Proc. R. Soc. London A* **202**, 81 (1950).

38. J. R. Melcher and M. Hurwitz, *J. Spacecraft Rockets* **4**, 863 (1967).

39. J. C. S. Meng and J. A. L. Thomson, *J. Fluid Mech.* **84**, 433 (1978).

40. R. Menikoff, R. C. Mjolsness, D. H. Sharp, and C. Zemach, *Phys. Fluids* **20**, 2000 (1977).

41. R. Menikoff, R. C. Mjolsness, D. H. Sharp, and C. Zemach, *Phys. Fluids* **21**, 1674 (1978).

42. R. Menikoff and C. Zemach, *J. Comput. Phys.* **51** 28 (1983).

43. K. A. Meyer and P. J. Blewett, *Phys. Fluids* **15**, 753 (1972).

44. M. Mitchner and R. K. M. Landshoff, *Phys. Fluids* **7** 862 (1964).

45. D. W. Moore, *SIAM J. Sci. Stat. Comput.* **2**, 65 (1981).

46. C. D. Munz and L. Schmidt, in *Nonlinear Hyperbolic Equations; Theory, Computational Methods and Applications*, edited by J. Ballman, R. Jeltsch, Notes on Numerical Fluid Mechanics, Vol. 24 (Friedrich Vieweg and Sohn, Braunschweig/Wiesbaden, 1989).

47. S. Osher and J. A. Sethian, *J. Comput. Phys.* **79** (1), 12 (1988).

48. S. Osher and F. Solomon, *Math. Comput.* **38**, 339 (1982).

49. S. Osher and P. K. Sweby, in *The Art of Numerical Analysis* (Clarendon Press, Oxford, 1987), p. 681.

50. M. S. Plesset and D. Y. Hsieh, *Phys. Fluids* **7**, 1099 (1964).

51. R. Popil and F. L. Curzon, *Phys. Fluids* **23** (8), 1718 (1980).

52. D. I. Pullin, *J. Fluid Mech.* **119**, 507 (1982).

54. L. Rayleigh, *Scientific Papers* (Cambridge Univ. Press, Cambridge, 1900), Vol. II, p. 200; *Proc. London Math. Soc.* **14**, 170 (1883).

55. K. I. Read, *Physica D* **12**, 45 (1984).

56. R. D. Richtmyer, *Commun. Pure Appl. Math.* **13**, 297 (1960).

57. P. L. Roe, *Annu. Rev. Fluid Mech.* **18**, 337 (1986).

58. P. G. Saffman and G. R. Baker, *Annu. Rev. Fluid Mech.* **11**, 95 (1979).

59. J. A. Sethian, "Computing the Motion of Curves and Evolving Surfaces," in *Geometric Motion*, edited by F. A. Almgren and J. Taylor (Amer. Math. Soc., Providence, RI, 1991.

60. J. A. Sethian, *Commun. Math. Phys.* **101**, 487 (1985).

61. J. A. Sethian, *J. Differential Geom.* **31**, 131 (1989).

62. J. A. Sethian and J. Strain, *J. Comput. Phys.*, (1990).

63. D. L. Sharp, in Fronts, Interfaces and Patterns, Proceedings of the Third International Conference of the Center for Nonlinear Studies, A. R. Bishop, L. J. Campbell, and P. J. Channell, Eds., North-Holland, Amsterdam, 1984.

64. C. W. Shu and S. Osher, *J. Comput. Phys.* **83**, 32 (1989).

65. G. I. Taylor, *Proc. R. Soc. London A* **201**, 192 (1950).

66. G. Tryggvason, *J. Comput. Phys.* **75**, 2 (1988).

67. B. Van Leer, in *Eighth International Conference on Numerical Methods in Fluid Dynamics*, edited by E. Krause, Lecture Notes in Physics, Vol. 170 (Springer-Verlag, New York/Berlin, 1982), p. 507.

68. K. H. Winkler, J. W. Chalmers, S. W. Hodson, P. R. Woodward, and N. J. Zabusky, *Phys. Today* **40**, 28 (1987).

69. D. L. Young, *Physica D* **12**, 32 (1984).

70. N. J. Zabusky and E. O. Overman, *J. Comput. Phys.* **52**, 351 (1984).